Agricultural and Forest Meteorology 388 (2026) 111370

Contents lists available at ScienceDirect

Agricultural and Forest Meteorology

journal homepage: www.elsevier.com/locate/agrformet

Mechanistic estimation of C_3 photosynthetic capacity in Chinese ecosystems using satellite SIF observations

Jingjing Yang [a,1], Zhunqiao Liu [a,1], Chenhui Guo [b], Qiang Yu [a], Shiwen Wang [a], Xiaoliang Lu [a,*]

[a] State Key Laboratory of Soil and Water Conservation and Desertification Control, College of soil and Water Conservation Science and Engineering (Institute of Soil and Water Conservation), Northwest A&F University, Yangling, Shaanxi, 712100, China
[b] College of Natural Resources and Environment, Northwest A&F University, Yangling, Shaanxi, 712100, China

ARTICLE INFO

Keywords:
Maximum carboxylation rate (V_{cmax})
Solar-Induced chlorophyll fluorescence (SIF)
Rubisco-limited photosynthesis
The fraction of open PSII reactions (q_L)
Leaf-level concurrent measurement system

ABSTRACT

Most terrestrial biosphere models utilize the Farquhar, von Caemmerer, and Berry (FvCB) model to estimate photosynthetic CO_2 assimilation. The maximum Ribulose-1,5-bisphosphate carboxylase/oxygenase (Rubisco) carboxylation rate at 25 °C (V_{cmax25}) is an essential parameter in the FvCB model. V_{cmax25} not only varies significantly across different plant functional types (PFTs), but also exhibits large variations even within the same PFT. Sun-induced chlorophyll fluorescence (SIF), an effective proxy for plant photosynthesis, has demonstrated strong potential for estimating V_{cmax25}. Specifically, when photosynthesis is Rubisco-limited, there is a mechanistic relationship between SIF and V_{cmax25}, with the fraction of open PSII reaction centers (q_L) being the key factor linking SIF to V_{cmax25}. Based on this relationship, we propose a mechanistic model for estimating V_{cmax25} at large scale. The canopy is first divided into two parts: sunlit and shaded leaves, and we find that photosynthesis in sunlit leaves is primarily Rubisco-limited. Building on the previous work, q_L can be effectively estimated from SIF and air temperature. Here, we employed a leaf-level concurrent measurement system to estimate key parameters in the SIF-based q_L estimation model for 45 plant species across 12 main PFTs in China. We applied the SIF-based model to derive V_{cmax25} across China at a 0.05-degree resolution at a daily scale from 2019 to 2022. The ecosystem-level V_{cmax25} in China showed significant variation among different vegetation types: cropland exhibited the highest mean annual V_{cmax25} (113.72 μmol m^{-2} s^{-1}), while boreal evergreen needleleaf forests had the lowest values (52.67 μmol m^{-2} s^{-1}). A comparison of our SIF-based V_{cmax} (V_{cmax_SIF}) values at the canopy level with V_{cmax} values derived from eddy covariance (V_{cmax_EC}), reveals that V_{cmax_SIF} explains approximately 86% of the variability in daily V_{cmax25_EC} at nine EC sites. Thus, we conclude that the method presented here offers an effective solution for the large-scale mechanistic estimation of V_{cmax}.

1. Introduction

The Farquhar, von Caemmerer, and Berry (FvCB) model is extensively employed to estimate the photosynthetic rates of C_3 plants (Farquhar et al., 1980). It predicts the rate of CO_2 assimilation in plant leaves as the smaller of two values: one governed by Rubisco carboxylation reactions, and the other by Ribulose-1,5-bisphosphate (RuBP) regeneration linked to the chloroplast electron transport rate. Within this framework, the maximum carboxylation rate (V_{cmax}) at a standard temperature (often 25°C; V_{cmax25}) is a key parameter that determines the photosynthetic capacity of plant leaves (Liu et al., 2024a). V_{cmax25} varies greatly between species, and, even within the same plant functional types (PFTs, Alton, 2018; Smith et al., 2019), it fluctuates significantly depending on environmental conditions and growth seasons (Liu et al., 2023).

A variety of satellite-based remote sensing methods have been proposed for large-scale estimation of V_{cmax25}. These approaches generally fall into three main categories. The first approach involves establishing statistical relationships between V_{cmax25} and various proxies, such as leaf chlorophyll content (LCC, Croft et al., 2017; Luo et al., 2019). However, it is important to note that challenges persist in establishing explicit mechanistic links between proxies like LCC to V_{cmax25}. Relying solely on statistical relationships to estimate V_{cmax25} across large spatial scales may introduce uncertainties. In particular, these approaches rely

* Corresponding author.
E-mail address: luxiaoliang@nwafu.edu.cn (X. Lu).
[1] These authors contributed equally to this work.

https://doi.org/10.1016/j.agrformet.2026.111370
Received 9 April 2025; Received in revised form 9 July 2026; Accepted 14 July 2026

on PFT-specific empirical coefficients—for example, the regression parameters used to derive V_{cmax25} from leaf chlorophyll—that are tied to predefined plant functional types and often calibrated on limited datasets, thereby constraining their ability to capture the spatiotemporal variations of V_{cmax25} (Chen et al., 2022).

The second category involves data assimilation approaches. Recent studies have highlighted the potential of solar-induced chlorophyll fluorescence (SIF) as a reliable indicator of plant photosynthetic rates (Yang et al., 2015) for estimating V_{cmax25}. For instance, He et al. (2019) proposed a data assimilation framework to constrain the Boreal Ecosystem Productivity Simulator (BEPS, Chen et al., 1999) by integrating SIF observations, thus optimizing V_{cmax25} within the FvCB model. Importantly, data assimilation represents a class of model-based inversion approaches whose performance is strongly conditioned by the underlying process model, the observation operator, and the assumptions made about prior information and error statistics. When the observation operator relies on empirical SIF–GPP relationships, seasonal variability can be underrepresented and application across broad spatial domains may lead to unrealistic adjustments in V_{cmax25} (He et al., 2019; Yu et al., 2024), and the computational cost can be substantial for multi-year runs.

The third approach establishes a mechanistic relationship between V_{cmax25} and SIF emission. Under Rubisco-limited conditions, SIF emitted by photosystem II (PSII), together with the fraction of open PSII reaction centers (q_L), provides a biophysically grounded constraint on V_{cmax25} (Han et al., 2022; Gu et al., 2019), offering a promising new approach for rapid estimation of V_{cmax25} at large scales. Although this method explicitly demonstrates the connection between SIF and V_{cmax25}, it remains constrained primarily to leaf-scale applications, posing challenges for large-scale implementation. To successfully estimate V_{cmax25} from SIF using this mechanistic framework, two critical aspects need to be addressed: (1) determining whether photosynthesis is Rubisco-limited, and (2) accurately estimating q_L.

In this study, we used a leaf-level measurement system (Liu et al., 2022) to estimate the necessary parameters for the SIF-based q_L estimation model for 45 different plant species across the 12 main PFTs in China. We also developed a method to determine whether photosynthesis is under the Rubisco-limited state. Using this framework, we obtained the spatially explicit V_{cmax25} for China with a 0.05° resolution at a daily time step from 2019 to 2022, and analyze the spatial and seasonal patterns of V_{cmax25} for the main PFTs. To evaluate the effectiveness of the proposed model, we used V_{cmax25} derived from eddy covariance measurements at nine study sites, representing four PFTs, as validation data. Finally, we compared the SIF-based V_{cmax} with two existing V_{cmax} products.

2. Methods and measurements

2.1. Model description

2.1.1. The mechanistic relationship between sunlit leaves V_{cmax25} and SIF

We invoked the temperature response function ($f_V(T)$) to obtain V_{cmax25} (Eq. 1a). According to Medlyn et al. (2002), $f_V(T)$ can be expressed with an Arrhenius function:

$$V_{cmax} = V_{cmax25} \times f_V(T) \tag{1a}$$

$$f_V(T) = e^{(T_{air}-25)\times E_{Vcmax} / \left[298 R_{gas} \times (T_{air}+273)\right]} \tag{1b}$$

where T_{air} (°C) is air temperature; E_{Vcmax} (J mol^{-1}) is the activation energy, defining the responsiveness of the relevant parameter to temperature, assumed to be 65,330 J mol^{-1} (Bernacchi et al., 2001); R_{gas} is the molar gas constant (8.3143 m^3 Pa mol^{-1} K^{-1}).

At the canopy scale, under well-watered conditions and when the rate of photosynthesis is Rubisco-limited, according to Han et al. (2022), the mechanistic link between V_{cmax25} and SIF is obtained by constraining the electron-transport term of the FvCB model with the actual electron transport rate (J_a) inferred from PSII SIF and the fraction of open PSII reaction centers q_L using the SIF-based MLR-SIF approach (Gu et al., 2019). Equating the SIF-diagnosed J_a with the FvCB expression and rearranging yields an explicit expression for V_{cmax25} as a function of q_L, SIF and gas-exchange variables:

$$Vcmax = \frac{Ci + KCO}{(4Ci + 8\Gamma^*)} \times \frac{\Phi PSIImax}{1 - \Phi PSIImax} \times (1 + KDF) \times qL \times SIFTOT\_FULL\_PSII \tag{2a}$$

$$Vcmax25 = \frac{1}{f_V(T)} \times \frac{Ci + KCO}{(4Ci + 8\Gamma^*)} \times \frac{\Phi PSIImax}{1 - \Phi PSIImax} \times (1 + KDF) \times qL \times SIFTOT\_FULL\_PSII \tag{2b}$$

where C_i (μbar) denotes the intercellular CO_2 concentration; K_{CO} (μbar) is an integrated factor for the Michaelis–Menten coefficients for RuBP carboxylation and oxygenation (Yin and Struik, 2009); Γ^* (μbar) is the chloroplastic compensation point of CO_2; q_L represents the proportion of open PSII reactions, and $\Phi_{PSIImax}$ refers to the maximum photochemical yield of the dark-acclimated leaves, generally assumed to be 0.80 (van der Tol et al., 2014); K_{DF} is defined as the ratio of the rate coefficients for inherent thermal dissipation and fluorescence, which is typically estimated to be 9.0 (Liu et al., 2022); $SIF_{TOT\_FULL\_PSII}$ (μmol m^{-2} s^{-1}) is the total SIF emission from Photosystem II in the range of 640-850 nm.

In the canopy, photosynthesis for all leaves is not universally Rubisco-limited, typically, it's the sunlit leaves that are more likely limited by Rubisco (Zheng et al., 2017). This study introduces a revised V_{cmax25} mechanistic estimation model, which enhances the calculation in two ways. First, by specifically differentiating between sunlit and shaded leaves, concentrating on calculating V_{cmax25} for sunlit leaves and, second, by incorporating the impact of soil water stress (Beauclaire et al., 2024; Cui et al., 2020), a factor not considered in the original model. Thus, the mechanistic model for estimating V_{cmax} (V_{cmax25}) of sunlit leaves at the canopy scale, accounting for water stress, becomes:

$$Vcmax = f_w \times \frac{Ci + KCO}{(4Ci + 8\Gamma*)} \times \frac{\Phi PSIImax}{1 - \Phi PSIImax} \times (1 + KDF) \times qL\_SUN \times SIFSUN\_FULL\_PSII \tag{3a}$$

$$Vcmax25 = f_w \times \frac{1}{f_V(T)} \times \frac{Ci + KCO}{(4Ci + 8\Gamma*)} \times \frac{\Phi PSIImax}{1 - \Phi PSIImax} \times (1 + KDF) \times qL\_SUN \times SIFSUN\_FULL\_PSII \tag{3b}$$

where f_w is an empirical function of soil moisture variation and can be expressed as a function of soil water content (SWC), SWC at field capacity (θ_F) and at the wilting point (θ_W) (Bu et al., 2024); q_{L_SUN} is q_L for sunlit leaves; $SIF_{SUN\_FULL\_PSII}$ (μmol m^{-2} s^{-1}) is the total PSII SIF emission from sunlit leaves. The methods for calculating f_w, C_i, Γ^*, and K_{CO} have been described in the previous study (Liu et al., 2022); for detailed steps, please refer to Text S1.

2.1.2. Estimation of q_{L_SUN}

Liu et al. (2024b) proposed a SIF-based, semi-empirical model to estimate q_{L_SUN}:

$$qL\_SUN = \frac{m}{\delta \times SIFSUN\_FULL\_PSII^{1/m} + m} \tag{4a}$$

$$m = m_{opt} \times \frac{H_d \times exp\left(\frac{H_a \times (T_{leaf} - T_{opt})}{T_{leaf} \times R_{gas} \times T_{opt}}\right)}{H_d - H_a \times \left(1 - exp\left(\frac{H_d \times (T_{leaf} - T_{opt})}{T_{leaf} \times R_{gas} \times T_{opt}}\right)\right)} \tag{4b}$$

where δ is a fixed value of 1 in units of μmol^{-1} m^2 s. To consider for the temperature sensitivity of q_{L_SUN}, a peaked function is used to describe m (Medlyn et al., 2002). T_{Leaf} (K) is leaf temperature; T_{opt} (K) refers to the optimal temperature for T_{Leaf}, and m_{opt} is the value of m at T_{opt}; H_d (kJ mol^{-1}) represents the rate at which the peak function decreases above T_{opt}, while H_a (kJ mol^{-1}) signifies the rate at which it increases below T_{opt}.

It should be noted that Eqs. (4a) & (4b) can be applied at both leaf and canopy scale. For canopy scale applications, one should use T_{air} instead of T_{Leaf}. This substitution is advised because of the challenges in precisely estimating T_{Leaf} distribution across the canopy.

2.1.3. Estimation of $SIF_{SUN\_FULL\_PSII}$

$SIF_{SUN\_FULL\_PSII}$ can be expressed as:

$$SIF_{TOT\_FULL\_PSII} = SIF_{SUN\_FULL\_PSII} \times LAI_{SUN} + SIF_{SHA\_FULL\_PSII} \times LAI_{SHA} \quad (5a)$$

$$SIF_{SUN\_FULL\_PSII} = APAR_{SUN} \times \beta_2 \times \Phi_{SUN\_SIF\_PSII} \quad (5b)$$

$$SIF_{SHA\_FULL\_PSII} = APAR_{SHA} \times \beta_2 \times \Phi_{SHA\_SIF\_PSII} \quad (5c)$$

where $APAR_{SUN}$ (μmol m^{-2} s^{-1}) represents the absorbed photosynthetically active radiation (PAR) for sunlit leaves; $APAR_{SHA}$ (μmol m^{-2} s^{-1}) represents the absorbed PAR for shaded leaves; LAI_{SUN} (m^2 m^{-2}) is the leaf area index (LAI, m^2 m^{-2}) for all sunlit leaves; LAI_{SHA} (m^2 m^{-2}) is the LAI for shaded leaves; $\Phi_{SUN\_SIF\_PSII}$ and $\Phi_{SHA\_SIF\_PSII}$ represent the quantum yields of PSII SIF emission of sunlit and shaded leaves, respectively; $SIF_{SHA\_FULL\_PSII}$ (μmol m^{-2} s^{-1}) represent the total PSII SIF emission from shaded leaves; β_2 is the fraction of APAR that is received by PSII, generally considered to be 0.5 (Galmés et al., 2007). Here, the ratio of $\Phi_{SUN\_SIF\_PSII}$ and $\Phi_{SHA\_SIF\_PSII}$ remains largely constant, being set at 1.1 (Guo et al., 2024), based on simulations conducted with the Soil Canopy Observation of Photosynthesis and Energy (SCOPE) model (version 1.73, van der Tol et al., 2009).

$APAR_{SUN}$ and $APAR_{SHA}$ can be estimated as (He et al., 2013):

$$APAR_{SUN} = (1-\alpha_L) \times PAR_{SUN} = (1-\alpha_L) \times \left(PAR_{DIR} \times \frac{\cos(\alpha)}{\cos(\theta)} + \frac{PAR_{DIF} \times P}{LAI_{SUN}} + C \right) \quad (6a)$$

$$APAR_{SHA} = (1-\alpha_L) \times PAR_{SHA} = (1-\alpha_L) \times \left(\frac{PAR_{DIF} \times (1-P) - PAR_{DIF\_UNDER}}{LAI_{SHA}} + C \right) \quad (6b)$$

where α_L is the albedo related to vegetation types (Table S1) (He et al., 2013); PAR_{SUN} (μmol m^{-2} s^{-1}) is PAR for sunlit leaves; PAR_{SHA} (μmol m^{-2} s^{-1}) is PAR for shaded leaves; PAR_{DIR} (μmol m^{-2} s^{-1}) represents the direct component of PAR; θ (°) represents the solar zenith angle; α (°) is the mean leaf-sun angle, which was assumed to be 60°–found to be a valid approximation when θ is within the range 30 to 60° (Chen et al., 1999); PAR_{DIF} (μmol m^{-2} s^{-1}) represents the diffuse component of PAR; PAR_{DIF_UNDER} (μmol m^{-2} s^{-1}) represents the portion of diffuse PAR beneath the plant canopy; P represents the probability of PAR_{DIF} being absorbed by sunlit leaves within the canopy; C (μmol m^{-2} s^{-1}) represents the multiple scattering of direct radiation. For the estimation of the above parameters PAR_{DIR}, PAR_{DIF}, PAR_{DIF_UNDER}, P, and C, please refer to Text S2.

LAI_{SUN} and LAI_{SHA} can be estimated as:

$$LAI_{SUN} = 2 \times \cos(\theta) \times \left(1 - \exp\left(\frac{-0.5 \times CI \times LAI}{\cos(\theta)} \right) \right) \quad (7a)$$

$$LAI_{SHA} = LAI - LAI_{SUN} \quad (7b)$$

where CI is the clumping index.

According to Yang et al. (2024), $SIF_{TOT\_FULL\_PSII}$ can be approximated as:

$$SIF_{TOT\_FULL\_PSII} = \sum_{\lambda=640}^{850} \left(\pi \times \frac{f_{PSII}(\lambda) \times SIF_{TOC\_\lambda}}{f_{esc\_P-C}} \times f_C(\lambda) \times \frac{\lambda \times 10^6}{h \times c \times N_A \times 10^3 \times 10^9} \right) \quad (8)$$

where λ (nm) is the wavelength; $f_{PSII}(\lambda)$ denotes the proportion of PSII SIF in relation to overall SIF emission at λ nm, which is determined in the leaf-level experiment (Table 1 and Text S3); SIF_{TOC_λ} (mW m^{-2} nm^{-1} sr^{-1}) is the top-of-canopy (TOC) SIF at a given wavelength λ nm; f_{esc_P-C} represents the likelihood that a SIF photon escapes from the PSII reactions within the leaves and reaches the canopy surface, and can be estimated from the vegetation far-red reflectance at the same wavelength as SIF_{TOC_λ} (R_{veg}), solar zenith angle (SZA, °), CI and LAI (see Supplementary Materials (Text S4) for details); h denotes the Planck constant; c is the speed of light; N_A is the Avogadro constant; 10^3, 10^9, and 10^6 are the conversion factors for physical units of milliwatts, nanometers, and micromoles, respectively; $f_C(\lambda)$ represents the proportion of SIF radiance at a specific wavelength, λ nm, relative to the total SIF emission integrated across the complete SIF range (640-850 nm). We used the SCOPE model to estimate $f_C(\lambda)$ (Liu et al., 2022).

2.2. Concurrent measurements of passive and active fluorescence and gas exchanges

At the leaf scale, we parameterized the SIF-based q_L predictive model by obtaining the overall broadband fluorescence emission from PSII ($SIF_{FULL\_PSII\_L}$, μmol m^{-2} s^{-1}), T_{Leaf}, and q_L across a range of light and temperature environments, thereby determining key parameters such as m_{opt}, T_{opt}, H_d, and H_a (Eqs. (4a) & (4b)). To enable the simultaneous measurement of pulse-amplitude modulation (PAM) fluorescence, passive fluorescence spectra, and leaf gas exchange, we developed an enhanced portable photosynthesis instrument (Fig. 1, LI-6800, LI-COR Inc.). We engineered two openings in the base plate of the leaf chamber and equipped them both with a fiber-optic cable, which are each connected to a separate QE-Pro spectrometer. These spectrometers both have a spectral resolution of approximately 0.2 nm, and cover the ranges 635.0-863.8 nm and 640.2-870.2 nm, respectively. Both spectrometers were radiometrically calibrated using an integrating sphere paired with a halogen light source and a spectroradiometer (QE-Pro, Ocean Optics Inc.), with the spectroradiometer also calibrated against a certified light source traceable to the National Institute of Standards and Technology (NIST). Upwelling and downwelling radiation were observed through an inclined fiber optic attached to the side-mounted lens (FX-SV1, Panasonic Inc.), featuring a 30° field of view (FOV) and a 45° viewing angle relative to the zenith, and an upward-facing bare fiber optic with a 25°FOV, respectively. The total leaf-scale fluorescence flux was calculated by summing the upward and downward fluorescence radiation (SIF_{up_λ} and SIF_{down_λ}, mW m^{-2} nm^{-1} sr^{-1}).

Using the previously described leaf-level concurrent measurement system (Fig. 1), we measured the light, CO_2, and temperature response curves of healthy mature leaves from 45 different plant species across 12 main PFTs at the Northwest A&F University Museum Garden. Notably, although the measurements were conducted in Yangling, the Garden's climate-controlled facilities provide water-thermal regimes aligned with species' ecological requirements, allowing expression of functional traits closer to those in native habitats and thereby offering a reasonably representative setting for sampling. After a one-hour dark adaptation, each chosen leaf was positioned in the chamber to measure dark respiration (R_d, μmol m^{-2} s^{-1}), as well as minimal and maximal fluorescence yields (F_o and F_m). Subsequently, we conducted the following measurements: (1) Light response curve: under a CO_2 level of 420 ppm, a T_{Leaf} at 25 °C, a stable relative humidity of 50%, and a consistent flow rate of 500 μmol s^{-1}, the light intensity was incrementally raised from 0 to 2100 μmol m^{-2} s^{-1} at the following values: 0, 30, 50, 100, 200, 400, 600, 900, 1200, 1500, 1800, and 2100 μmol m^{-2} s^{-1}; (2) On the same leaf,

Table 1
Plant species, abbreviations, corresponding plant functional types (PFTs), and fitted parameters for the proposed SIF-based V_{cmax} estimation model. T_{opt} (°C): the optimal temperature for T_{Leaf}; m_{opt}: the value of m at T_{opt}; H_d (kJ mol^{-1}): the rate at which the peak function decreases above T_{opt}; H_a (kJ mol^{-1}): the rate at which it increases below T_{opt}; f_{PSII}(743): the proportion of PSII SIF in relation to overall SIF emission at λ nm, which was determined in the leaf-level experiment (see Text S3). (BoC_3GRA: boreal C_3 grass; BoDBF: boreal deciduous broadleaf forest; BoDBSH: boreal deciduous broadleaf shrub; BoDNF: boreal deciduous needleleaf forest; BoENF: boreal evergreen needleleaf forest; C_3GRA: C_3 grass; CRO: crops; TeDBF: temperate deciduous broadleaf forest; TeDBSH: temperate deciduous broadleaf shrub; TeEBF: temperate evergreen broadleaf forest; TeENF: temperate evergreen needleleaf forest; TrEBF: tropical evergreen broadleaf forest).

Abbreviation/PFTs	Species	m_{opt}	H_d (kJ mol^{-1})	H_a (kJ mol^{-1})	T_{opt} (°C)	f_{PSII}(743)
LSL	wild lettuce (*Lactuca serriola L*)	2.06	659.04	21.9409	41.76	0.38
OBL	*Ophiopogon bodinieri Levl.*	1.08	165.17	18.2856	35.82	0.35
ABB	*Achyranthes bidentata Blume*	1.23	171.52	14.8529	37.09	0.41
BoC_3GRA	**Species Mean**	**1.46**	**331.91**	**18.36**	**38.22**	**0.38**
XSB	Yellowhorn (*Xanthoceras sorbifolium Bunge*)	1.56	143.29	20.3752	37.46	0.41
FMR	Manchurian ash (*Fraxinus mandshurica Rupr.*)	1.11	177.52	12.0829	33.42	0.44
RPI	Black locust (*Robinia pseudoacacia cv. idaho*)	2.49	332.94	24.6141	40.3	0.41
BoDBF	**Species Mean**	**1.72**	**217.92**	**19.02**	**37.06**	**0.42**
ANL	Box elder (*Acer negundo L.*)	1.16	157.42	17.9438	35.36	0.34
PSB	*Periploca sepium Bunge*	1.3	115.44	16.7813	31.34	0.45
CAA	Tatarian dogwood (*Cornus alba Linnaeus*)	2.42	301.33	23.7086	37.43	0.36
BoDBSH	**Species Mean**	**1.63**	**191.40**	**19.48**	**34.71**	**0.38**
MGC	Dawn redwood (*Metasequoia glyptostroboides Hu & W. C. Cheng*)	0.97	192.75	11.7421	36.78	0.45
PPZ	Japanese white pine (*Pinus parviflora Siebold et Zuccarini*)	1.52	446.13	22.1218	39.4	0.42
PAR	Golden larch (*Pseudolarix amabilis (Nelson) Rehd.*)	1.7	231.94	38.842	32.96	0.31
BoDNF	**Species Mean**	**1.40**	**290.27**	**24.24**	**36.38**	**0.39**
PBZ	Lacebark pine (*Pinus bungeana Zucc.*)	1.09	203.4	14.3203	35.18	0.45
PTP	Japanese black pine (*Pinus thunbergii Parl.*)	1.05	146.16	13.8964	39.73	0.32
PSL	Mongolian Scots pine (*Pinus sylvestris var. mongholica Litv.*)	1.72	2519.82	14.3165	43.65	0.42
AFC	*Abies fabri Craib*	1.18	248.7	17.4665	36.05	0.4
BoENF	**Species Mean**	**1.26**	**779.52**	**15.00**	**38.65**	**0.40**
SLT	*Solanum lyratum Thunb.*	1.67	217.66	20.5513	36.28	0.43
PAL	Pokeweed (*Phytolacca americana L.*)	2.17	192.28	23.0182	41.06	0.42
ITM	Roof iris (*Iris tectorum Maxim.*)	1	176.82	18.0262	34.55	0.34
FTB	*Ficus tikoua Bur.*	2.23	258.1	22.884	37.17	0.4
CJG	*Cayratia japonica (Thunb.) Gagnep.*	1.5	184.05	17.31	38.87	0.4
CIL	*Canna indica L.*	1.74	112.58	21.82	30.99	0.4
C_3GRA	**Species Mean**	**1.61**	**195.59**	**20.53**	**36.49**	**0.40**
GMM	Soybean (*Glycine max (L.) Merr.*)	1.63	212.66	12.256	35.01	0.44
TAL	Common wheat (*Triticum aestivum L.*)	2.58	2800	14.5	43.08	0.45
BVL	Beet (*Beta vulgaris L.*)	1.76	235.76	20.1987	40.3	0.4
CAL	Pepper (*Capsicum annuum L.*)	1.35	91.03	29.8799	36.8	0.33
ZML	Maize (*Zea mays L.*)	2.13	2472.76	19.7831	43.69	0.49
PIL	Foxtail millet (*Panicum italicum L.*)	1.98	141.72	12.9134	37.32	0.43
SBM	Sorghum (*Sorghum bicolor Moench*)	2.23	152.91	26.3072	38.81	0.46
OSL	Rice (*Oryza sativa L.*)	2.69	2070	22.63	38.71	0.34
CRO	**Species Mean**	**2.04**	**1022.73**	**19.64**	**39.22**	**0.42**
ACB	Chinese horse chestnut (*Aesculus chinensis Bunge*)	1.13	191.02	10.4907	35.23	0.44
RPL	Black locust (*Robinia pseudoacacia L.*)	1.53	195.59	15.7094	35.33	0.47
PRL	Peach (*Prunus persica L.*)	2.55	519.82	25.9819	41.36	0.38
TeDBF	**Species Mean**	**1.74**	**302.14**	**17.39**	**37.31**	**0.43**
PSA	Tree peony (*Paeonia suffruticosa Andrews*)	1.85	230.03	23.626	37.68	0.36
VMH	*Viburnum melanocarpum Hsu*	1.35	218.71	31.9224	34.68	0.29
AMS	*Armeniaca mume* Sieb.	2.26	1973.77	17.6973	43.54	0.42
TeDBSH	**Species Mean**	**1.82**	**807.50**	**24.42**	**38.63**	**0.36**
EJL	Loquat (*Eriobotrya japonica (Thunb.) Lindl.*)	2.49	349.86	27.888	38.63	0.37
OFL	*Osmanthus fragrans (Thunb.) Lour.*	0.98	157.43	12.2588	34.79	0.42
MGL	Southern magnolia (*Magnolia grandiflora L*)	1.55	205.68	23.3	38.26	0.36
TeEBF	**Species Mean**	**1.67**	**237.66**	**21.15**	**37.23**	**0.38**
PML	Masson pine (*Pinus massoniana Lamb.*)	1.35	164.85	15.8966	37.85	0.46
CDD	Deodar cedar (*Cedrus deodara (Roxb.) G. Don*)	1.33	176.13	18.9303	39.15	0.41
CLH	China fir (*Cunninghamia lanceolata (Lamb.) Hook.*)	1.11	174.82	23.7519	35.6	0.41
TeENF	**Species Mean**	**1.26**	**171.93**	**19.53**	**37.53**	**0.43**
LLA	Glossy privet (*Ligustrum lucidum Ait.*)	1.69	260.42	22.3331	37.11	0.36
TFW	Windmill palm (*Trachycarpus fortunei (Hook.) H. Wendl.*)	1.16	92.46	25.5326	32.19	0.42
SHF	*Schefflera heptaphylla (Linnaeus) Frodin*	1.11	175.41	16.8887	35.58	0.42
TrEBF	**Species Mean**	**1.32**	**176.10**	**21.58**	**34.96**	**0.40**

the CO_2 response curve was measured: at a saturated light intensity of 1500 μmol m^{-2} s^{-1} and a constant $T_{Leaf,}$ of 25°C, the CO_2 concentration was adjusted to the following levels: 420, 300, 200, 100, 30, 400, 600, 900, 1200, and 1500 μmol mol^{-1}; (3) the $T_{Leaf,}$ in the gas chamber was adjusted to 15°C, and, once steady-state photosynthesis was achieved (approximately 20 minutes), the temperature response curve was measured on the same leaf with a temperature sequence of 15, 20, 25, 30, 35, 40, and 45°C, conducted at a saturated light intensity of 1500 μmol m^{-2} s^{-1} and a stable CO_2 level of 420 ppm.

Throughout the experimental process, we used a spectroradiometer to simultaneously capture SIF_{up_λ} and SIF_{down_λ}, with optimal integration times set for each light level, CO_2 level, and T_{Leaf}. We also recorded the steady-state fluorescence yield (F_s), light-adapted maximum fluorescence yield (F_m'), and various gas exchange variables, including net photosynthetic CO_2 assimilation (A_n, μmol m^{-2} s^{-1}), C_i and T_{Leaf}. Maintaining the consistency of the measured leaf's position was crucial to ensure that the FOV of the spectroradiometer remained consistent across all different response curve measurements. In addition, we measured the

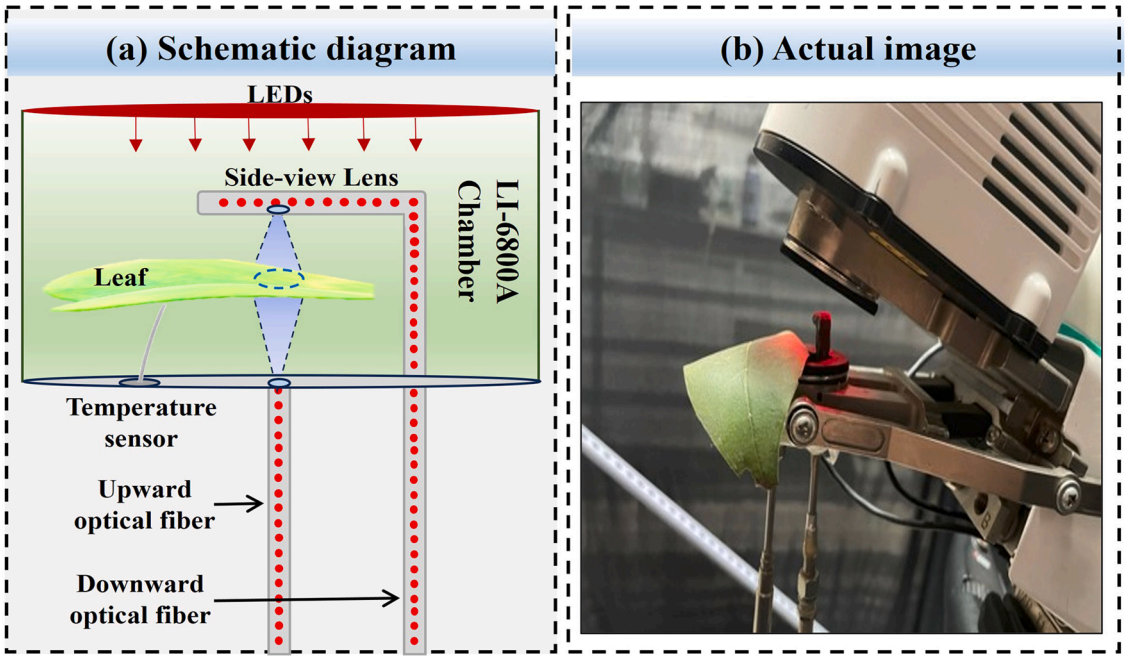

Fig. 1. Diagram of the system for simultaneous leaf-level measurements. (a) Illustration of the leaf chamber equipped with two optical fibers for capturing upward and downward fluorescence flux; (b) Image of the customized LI-6800 leaf chamber.

reflectance (R_λ) and transmittance (T_λ) of the same leaf using an ASD integrating sphere and a PSR+3500 high resolution portable spectrophotometer.

2.3. Determine the Rubisco-limited state

When estimating V_{cmax25} using Eq. (1), it is necessary first to determine whether photosynthesis is under the Rubisco-limited state. To do so, we propose a method based on the FvCB model to identify the photosynthetic limitation stage. According to the FvCB model, the photosynthetic rate of the canopy sunlit leaves can be estimated as the minimum of the Rubisco limited rate of CO_2 assimilation (A_c, μmol m^{-2} s^{-1}), and the electron transport limited rate of CO_2 assimilation (A_j, μmol m^{-2} s^{-1}), expressed as:

$$Ac = \frac{Vcmax \times (Ci - \Gamma^*)}{Ci + K_{CO}} \tag{9a}$$

$$Aj = \frac{J}{4} \times \frac{Ci - \Gamma^*}{Ci + 2\Gamma^*} \tag{9b}$$

$$J = \frac{\sigma \times PAR_{SUN} + J_{max} - \sqrt{(\sigma \times PAR_{SUN} + J_{max})^2 - 4\theta_J \times \sigma \times PAR_{SUN} \times J_{max}}}{2\theta_J} \tag{9c}$$

where J (μmol m^{-2} s^{-1}) is the electron transport rate; J_{max} (μmol m^{-2} s^{-1}) is the maximum electron transport rate; θ_J is an empirical curvature parameter and was fixed at 0.9 (Medlyn et al., 2002); σ is the product of $\Phi_{PSIImax}$, leaf light absorptance and fraction of absorbed photons allocated to PSII, which was set to 0.3 (Long et al., 1993). Note that the values of θ_J and σ have only a slight effect on the estimated value of J_{max} (Medlyn et al., 2002).

According to Eq. (1a) and the study by Yin and Struik. (2009), V_{cmax} and J_{max} can be expressed as functions of V_{cmax25} and J_{max} at a standard temperature (J_{max25}, μmol m^{-2} s^{-1}).

$$J_{max} = J_{max25} \times e^{(T_{air}-25)\times E_{Jmax} / [298 R_{gas} \times (T_{air}+273)]} \times \frac{1 + e^{(298 S_{Jmax} - D_{Jmax}) / (298 R_{gas})}}{1 + e^{[(T_{air}+273)\times S_{Jmax} - D_{Jmax}] / R_{gas} \times (T_{air}+273)}} \tag{10}$$

where S_{Jmax} (J K^{-1} mol^{-1}) is the entropy term, assumed to be 650 J K^{-1} mol^{-1} (Harley et al., 1992); E_{Jmax} and D_{Jmax} (J mol^{-1}) are the energies of activation and deactivation, defining the responsive shape of the sub and supra-optimal ranges, respectively. According to Yin et al. (2004) and Medlyn et al. (2002), E_{Jmax} and D_{Jmax} are typically set to 52, 970 J mol^{-1} and 200, 000 J mol^{-1}, respectively.

For C_3 plants, J_{max25} and V_{cmax25} often covary at a common reference temperature, and the ratio J_{max25}/V_{cmax25} has been parameterized as a function of plant growth temperature in previous studies, with an offset of 2.59 and a slope of -0.035 (Bacour et al., 2019, Kattge and Knorr, 2007). In this study, we adopted this relationship as an auxiliary constraint to derive the threshold V_{cmax25_FvCB} for diagnosing whether photosynthesis is Rubisco-limited. Under this parameterization, both V_{cmax} and J_{max} can be expressed as functions of V_{cmax25}. Furthermore, we can express both A_c and A_j as functions of V_{cmax25}:

$$Ac = \frac{Vcmax25 \times e^{(T_{air}-25)\times E_{Vcmax} / [298 R_{gas} \times (T_{air}+273)]} \times (Ci - \Gamma^*)}{Ci + K_{CO}} \tag{11a}$$

$$Aj = \frac{\sigma \times PAR_{SUN} + J_{max} - \sqrt{(\sigma \times PAR_{SUN} + J_{max})^2 - 4\theta_J \times \sigma \times PAR_{SUN} \times J_{max}}}{8\theta_J} \times \frac{Ci - \Gamma^*}{Ci + 2\Gamma^*} \tag{11b}$$

$$J_{max} = (2.59 Vcmax25 - 0.035) \times e^{(T_{air}-25)\times E_{Jmax} / [298 R_{gas} \times (T_{air}+273)]} \times \frac{1 + e^{(298 S_{Jmax} - D_{Jmax}) / (298 R_{gas})}}{1 + e^{[(T_{air}+273)\times S_{Jmax} - D_{Jmax}] / R_{gas} \times (T_{air}+273)}} \tag{11c}$$

For Eqs. (11a) and (11b), V_{cmax25} is the only unknown parameter, while all other variables can be derived from observations including T_{air}, dew point temperature (T_d,°C), incoming solar shortwave radiation (S_G,

W m^{-2}), CI, and LAI. Moreover, we can derive a threshold for V_{cmax25}, denoted as V_{cmax25_FvCB}, at which A_j and A_c become equal. This threshold serves as a key criterion for identifying the photosynthetic limitation stage. Specifically, if the V_{cmax25} estimated from Eq. (2b) is lower than V_{cmax25_FvCB}, photosynthesis is primarily Rubisco-limited, and the estimated V_{cmax25} is considered valid. Conversely, if the estimated V_{cmax25} exceeds V_{cmax25_FvCB}, photosynthesis is mainly limited by electron transport, and the corresponding V_{cmax25} estimate should be excluded. The spatial distribution of the percent of photosynthetic rate under the Rubisco-limited state from 2019 to 2022 is shown in Fig. S1. The procedure for quantifying V_{cmax25} from the observed SIF is shown in Fig. 2.

3. Data

3.1. Input data for estimating China V_{cmax25}

3.1.1. Leaf-level measurements

Liu et al. (2024b) demonstrated that the relationship between $SIF_{SUN\_FULL\_PSII}$ and q_{L_SUN} can be represented by a temperature-dependent parameter, m (Eq. (4a)). Based on this, we collected a total of 45 different plant leaves from the Northwest A&F University Botanical Garden, representing 12 PFTs. Utilizing the leaf-level concurrent measurement system (Fig. 1), we conducted measurements to acquire the necessary data for estimating q_L based on PAM fluorescence signals (q_{L_PAM}) and $SIF_{FULL\_PSII\_L}$, including passive fluorescence spectra, active fluorescence parameters, and gas exchange data. By measuring q_{L_PAM} and $SIF_{FULL\_PSII\_L}$ at different temperatures, we determined the specific m values for each temperature. These m values, along with their corresponding temperatures, subsequently facilitate the determination of the key parameters in Eq. (4b), namely m_{opt}, T_{opt}, H_d, and H_a, through nonparametric regression ('fitnlm' in MATLAB 2023b, MathWorks, Natick, MA, USA) for 12 different plant species (Table 1). For the estimation of the above parameters, q_{L_PAM} and $SIF_{FULL\_PSII\_L}$, please see Text S3.

3.1.2. Satellite data

We utilized SIF observations derived from the TROPOMI spectrometer on board the Sentinel-5 Precursor satellite, which crosses the equator at 13:30 local solar time and has a 16-day orbital period (Guanter et al., 2021). TROPOMI has a wide swath of 2600 km, enabling near-daily global coverage with a high spatial resolution of 7 × 3.5 km^2 at nadir (Köhler et al., 2018). Our analysis is based on the collection of instantaneous TROPOMI L2B data from the 743-758 nm window, spanning the period from January 2019 to December 2022. The SZA required for calculating $APAR_{SUN}$ and $APAR_{SHA}$ was also obtained from the TROPOMI L2B dataset (Guanter et al., 2021).

In addition to the previously mentioned data, our study incorporated three additional Moderate Resolution Imaging Spectroradiometer (MODIS) data products. LAI and f_{APAR} were retrieved from the MCD15A3H (version 6.1) dataset, which provides data every four days at a spatial resolution of 500 m (Myneni et al., 2021). To ensure data quality, we excluded observations influenced by cloud contamination and other noise, based on the dataset's quality control flags. The CI data were obtained from a global foliage clumping index map based on the MODIS bidirectional reflectance distribution function (BRDF) product at a 500-m spatial resolution (He et al., 2012).

For the land cover component, we used the 1-km resolution plant functional types map of China developed by Ran et al. (2012), which is accessible on the Big Earth Data for Three Poles (https://poles.tpdc.ac.cn/zh-hans/data/ab193a70-63a5-4df6-9bc1-d9b5ac5fb044/).

3.1.3. Meteorological data

For the SIF-driven V_{cmax25} simulation in China, the required meteorological inputs consist of T_{air}, T_d and S_G (Text S2). The vapor pressure deficit (VPD, kPa), utilized for estimating C_i (Text S1), was derived from T_{air} and T_d according to the methodology described by Wu et al. (2019).

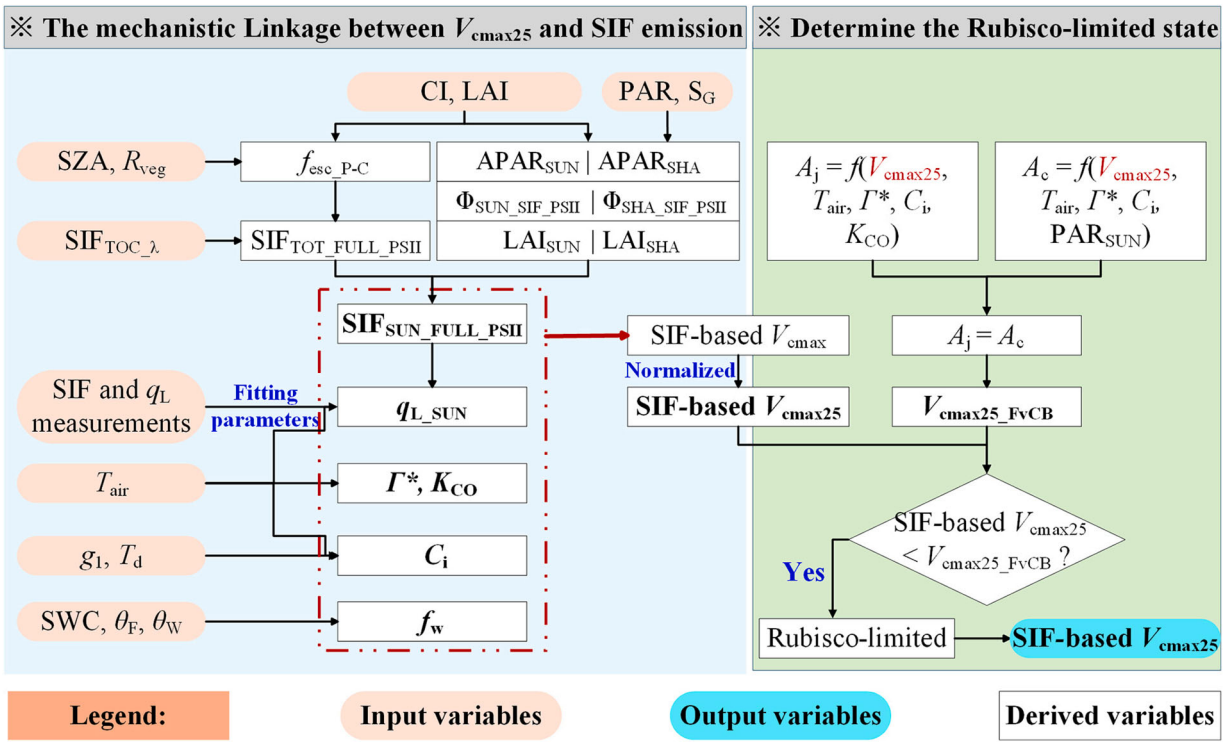

Fig. 2. Workflow of the SIF-based ecosystem V_{cmax25} model. The framework integrates satellite SIF observations, canopy structural variables, meteorological data, soil water information, and land-cover data at a spatial resolution of 0.05°. First, top-of-canopy SIF is converted into the total PSII SIF emission from sunlit leaves. The converted PSII SIF is then combined with the q_L estimation model to estimate q_L for sunlit leaves. Subsequently, SIF-based sunlit-leaf V_{cmax25} is calculated. Finally, a Rubisco-limitation diagnosis based on the FvCB model is applied to retain valid V_{cmax25} estimates and generate daily ecosystem V_{cmax25}.

Hourly datasets for T_{air}, T_d, and S_G were sourced from ERA5-Land (Muñoz-Sabater et al., 2021), the fifth generation of the European Reanalysis from the European Center for Medium-Range Weather Forecasts. ERA5-Land is a reanalysis dataset offering high-resolution (~9 km) hourly surface variable information from 1950 to the near present (Ma et al., 2022).

The soil hydraulic properties, θ_F and θ_W, were derived from the global database developed by Montzka et al. (2017), accessible via https://doi.pangaea.de/10.1594/PANGAEA.870605. This database provides a variety of key soil hydraulic parameters at seven predefined depths (0, 5, 15, 30, 60, 100, and 200 cm) at a resolution of 0.25°. For our analysis, we focused on the weighted averages in the top 100 cm of soil. We obtained hourly simulated volumetric soil water content (θ_S) from the ERA5-Land dataset. Simulated θ_S is available at five depths in this dataset (0, 7, 28, 100, and 289 cm) (Muñoz-Sabater et al., 2021). We used the depth-weighted mean of daytime SWC across the top three soil layers (0-100 cm).

3.1.4. Pre-processing input data

3.1.4.1. Temporal processing. We directly extracted instantaneous TROPOMI SIF, R_{veg} and SZA at ~13:30 local time without temporal aggregation. For T_{air}, T_d and S_G, we extracted the values at 13:00 and 14:00 local time and calculated their mean to synchronize with the 13:30 instantaneous SIF data. For the 4-day composite LAI and f_{APAR}, we applied a linear temporal interpolation to rescale them into daily estimates, and subsequently smoothed the LAI and f_{APAR} time series with a Savitzky–Golay filter. The land cover and CI data were assumed to remain unchanged throughout the study period.

3.1.4.2. Spatial resampling to 0.05°. The instantaneous TROPOMI SIF, R_{veg} and SZA were gridded to a spatial resolution of 0.05 degree using the GriddingMachine tool (Wang et al., 2022b). Variable-specific strategies were then applied to other inputs: datasets originally coarser than 0.05° (T_{air}, T_d, S_G, SWC, θ_F, and θ_W) were bilinearly interpolated to 0.05°. Products finer than 0.05° (LAI, f_{APAR}) were aggregated by area-weighted averaging to 0.05°. Land cover was resampled using nearest-neighbor/majority assignment. The detailed workflow for data processing is illustrated in Fig. 3. Definitions of symbols and units used in this study are outlined in Appendix A.

3.2. Site description

Zheng et al. (2017) showed that V_{cmax} can be reliably inverted from eddy covariance (EC) flux measurements. Initially, the GPP for sunlit leaves (GPP_{SUN}) was estimated through light response curves, a process which requires inputs including GPP, LAI_{SUN}, LAI_{SHA}, $APAR_{SUN}$, $APAR_{SHA}$, and θ. Subsequently, V_{cmax} was inferred from GPP_{SUN} using the F_VCB model. Therefore, the EC-derived V_{cmax} used here should be regarded as a model-derived benchmark rather than a direct physiological measurement of photosynthetic capacity. Here, we evaluated the SIF-based V_{cmax} (V_{cmax_SIF}) at the canopy level by comparing its output against EC-derived V_{cmax} (V_{cmax_EC}) values across various ecosystems, including cropland, grassland, and forest (Fig. 4, Table 2) for which EC measurements were available from January 2019 to December 2022. The site measurement data used for estimating V_{cmax_EC} were specifically chosen to coincide with the satellite overpass time (13:30).

Our selection of sites includes cropland: Changling (CL), Gucheng (GC), and Yangling (YL); grassland: Haibei (HB), Ruoergai (REG), and Panjin (PJ); and forest: Xiaolangdi (XLD), Puding (PD), and Yanshan (YS) (Fig. 4, Table 2). Data from the Yangling site were directly collected by our research team. The other site data were all sourced from the National Ecosystem Science Data Center (https://www.nesdc.org.cn/sdo/list), with the exception of the data from Xiaolangdi, which were obtained from ChinaSpec (http://chinaspec.nju.edu.cn/).

The cropland sites are located in distinct climatic zones (Fig. 4, Table 2). The CL site exemplifies a typical temperate continental climate. The soil is predominantly soda saline-alkali, making it primarily suitable for rice cultivation. The rice cultivation cycle at CL is structured into four phases: the nursery period from late March to early April, transplanting around May 10th, heading in mid-July, and harvesting by the end of September (Huang et al., 2024). The GC site is distinguished by its warm temperate continental monsoon climate. The station exemplifies a winter wheat-summer corn double-cropping system, facilitating two harvests annually. Winter wheat is typically sown around October 20th each year and harvested around June 10th. Ground-based

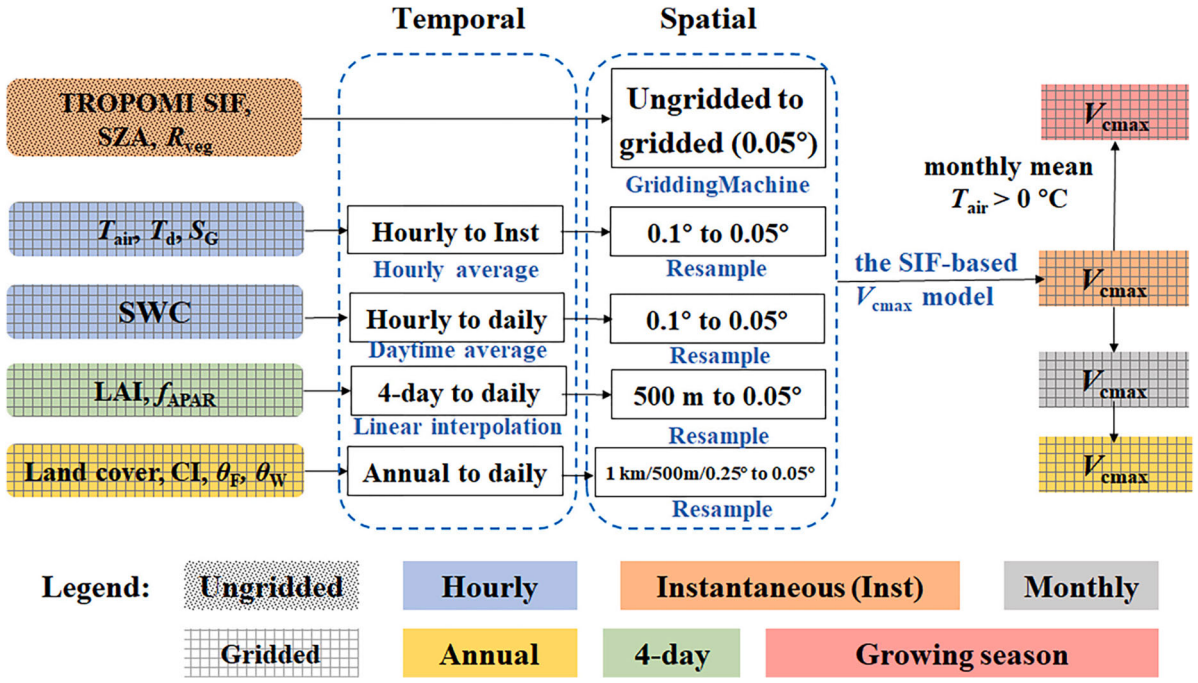

Fig. 3. Overview of the data processing workflow.

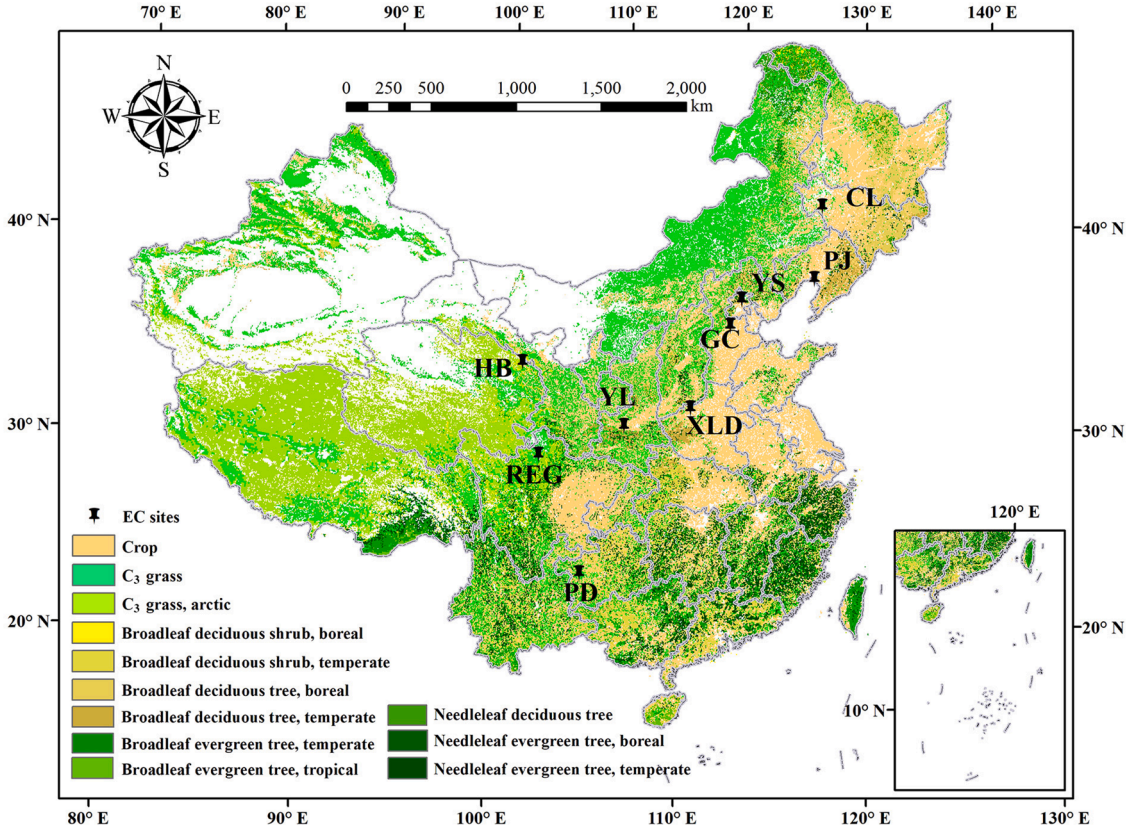

Fig. 4. The distribution of eddy covariance study sites across China used for validation in this study. Site names are provided in Table 2. The base map shows plant functional types at 1 km resolution (Ran et al., 2012).

Table 2
The eddy covariance sites. From left to right: site name; ID; plant functional types (PFTs); longitude (Lon. °); latitude (Lat. °); mean annual precipitation (MAP, mm); mean annual temperature (MAT,°C); time period. (CRO: crops; BoC_3GRA: boreal C_3 grass; TeC_3GRA: temperate C_3 grass; TeDBF: temperate deciduous broadleaf forest; TeENF: temperate evergreen needleleaf forest).

Site name	Site ID	PFTs	Lon. (°)	Lat. (°)	MAP (mm)	MAT (°C)	Time period
Changling	CL	CRO	123.4703	44.5967	375	5.5	2019.01-2020.12
Gucheng	GC	CRO	115.6667	39.1333	528	12.2	2020.01-2022.11
Yangling	YL	CRO	108.0682	34.2998	630	12.9	2022.02-2022.06
Haibei	HB	BoC_3GRA	101.3120	37.6094	535	-1.2	2019.05-2020.10
Ruoergai	REG	BoC_3GRA	102.5500	32.8000	749	1.4	2020.04-2020.10
Panjin	PJ	TeC_3GRA	121.9646	40.9327	631	8.6	2019.01-2020.12
Xiaolangdi	XLD	TeDBF	112.4690	35.0290	642	12.4	2019.01-2019.12
Puding	PD	TeENF	105.1319	26.6000	1432	16.0	2019.01-2019.12
Yanshan	YS	TeENF	116.6588	40.4165	635	11.1	2020.01-2021.12

measurements at the site commenced on February, 2022, and concluded shortly before the harvest in June, 2022 (Liu et al., 2024b).

The three grassland sites encompass two alpine meadows (HB, REG) and one temperate grassland (PJ) (Fig. 4, Table 2). The HB station is characterized by a distinct plateau continental climate. The primary vegetation is *Kobresia humilis*, a community-forming species in alpine meadows, and the soil type is typical of a subalpine meadow soil (Wang et al., 2021). REG has a highland cold temperate monsoon climate. The vegetation beneath the tower primarily consists of herbaceous marshes, with the dominant species being Muli sedge (*Carex muliensis*) and Tibetan kobresia (*Kobresia tibetica*) (Guo et al., 2021). The PJ site falls within a temperate semi-humid monsoon climate zone. The topography is dominated by alluvial plains and tidal flats, with reeds being the dominant species.

There are three forest sites: XLD is temperate deciduous broadleaf forest, while PD and YS are temperate evergreen needleleaf forest (Fig. 4, Table 2). The XLD site is primarily covered by Chinese cork oak (*Quercus variabilis*). The 32-year-old mixed plantation spans approximately 7,210 ha, with a stand density of 1,905 trees per ha (Tong et al., 2019). The PD site spans approximately 168 acres and is characterized by a humid subtropical monsoon climate. The vegetation is predominantly composed of subtropical species, with Chinese fir (*Cunninghamia lanceolata*) being the primary tree species (He et al., 2022). The YS site has a temperate climate and the region's natural vegetation is primarily composed of secondary forest dominated by Pinus tabulaeformis (Chinese pine).

4. Results

4.1. The performance in estimating leaf-scale q_L

Overall, q_{L_PAM} decreased with increasing light intensity across all plant species (Fig. 5), but the rate of decline varied among the different PFTs. BoC_3GRA (Fig. 5a), BoENF (Fig. 5e), TeENF (Fig. 5k), and TrEBF

(Fig. 5l) showed the fastest decreases, with q_{L_PAM} dropping from 1 to below 0.2 as light intensity increased from 0 to 900 μmol m^{-2} s^{-1} (Table S2). In contrast, in BoDBF (Fig. 5b), BoDBSH (Fig. 5c), BoDNF (Fig. 5d), C_3GRA (Fig. 5f), CRO (Fig. 5g), TeDBF (Fig. 5h), and TeEBF (Fig. 5j) q_{L_PAM} decreased more slowly, reaching values of 0.22 to 0.28 at the same light intensity (Table S2). Notably, q_{L_PAM} declined slowest in TeDBSH (Fig. 5i), remaining above 0.3 at 900 μmol m^{-2} s^{-1} (Table S2). Additionally, the minimum q_{L_PAM} varied among species (Fig. 5): when PAR exceeded 1800 μmol m^{-2} s^{-1}, the q_{L_PAM} of BoC_3GRA (Fig. 5a) dropped below 0.1, whereas for TeDBSH (Fig. 5i), it remained close to 0.2 (Table S2).

The predictive q_L models for different PFTs varied in their ability to capture the response of q_{L_PAM} to light intensity changes (Fig. 5). For C_3GRA and CRO, the models had high explanatory power, accounting

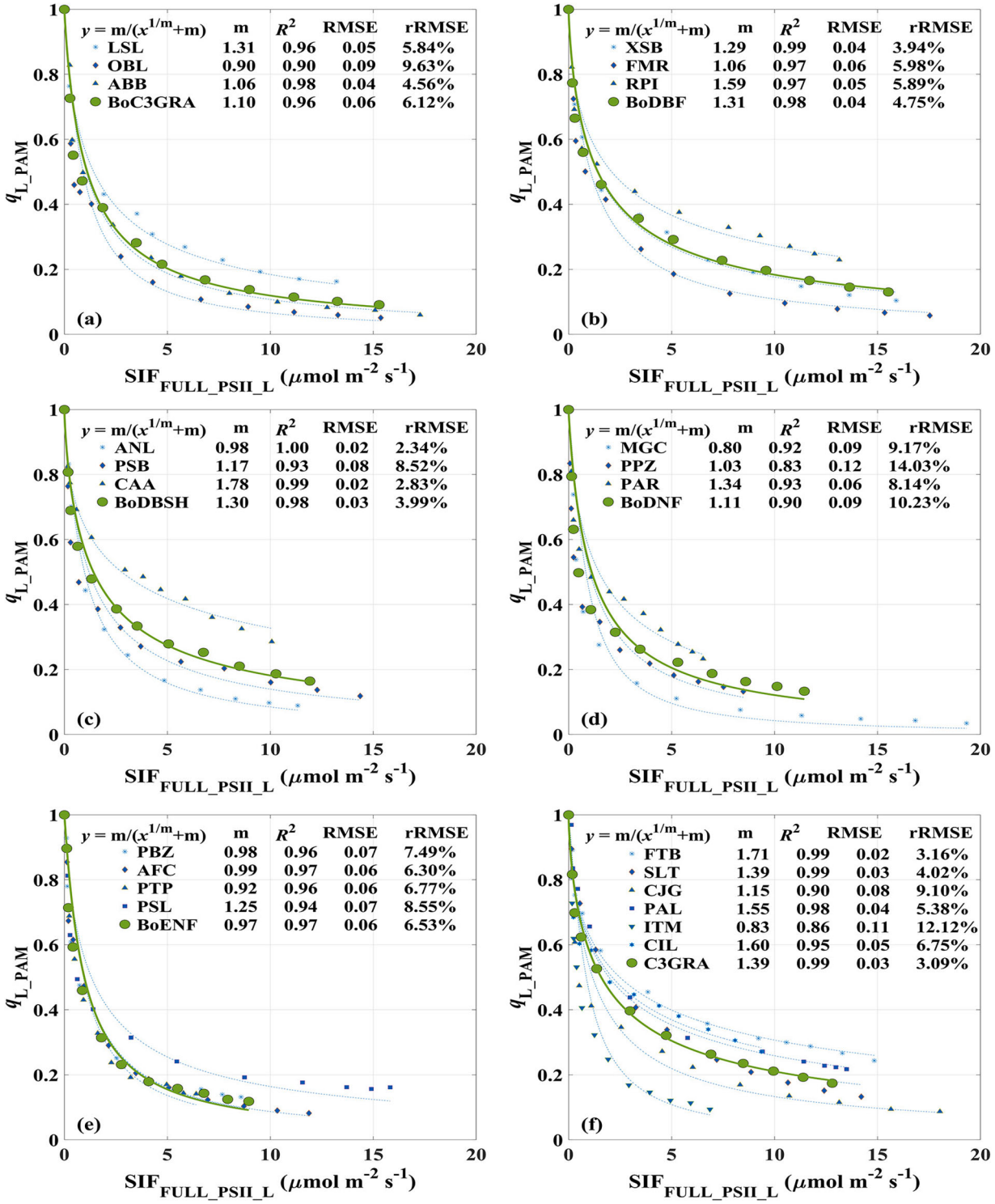

Fig. 5. Response curves of q_{L_PAM} to $SIF_{FULL\_PSII\_L}$ generated by fitting a hyperbolic function to the light response data for 45 plant species across 12 plant functional types (PFTs) at a temperature of 25 °C (Table 1). The thin and bold curves represent individual species and the mean of all species, respectively, for each PFT. q_{L_PAM} is obtained from PSI fluorescence-corrected data measured with a PAM fluorometer; $SIF_{FULL\_PSII\_L}$ is the total PSII fluorescence emission, determined from the upward and downward measurements of fluorescence radiance (μmol m^{-2} s^{-1}).

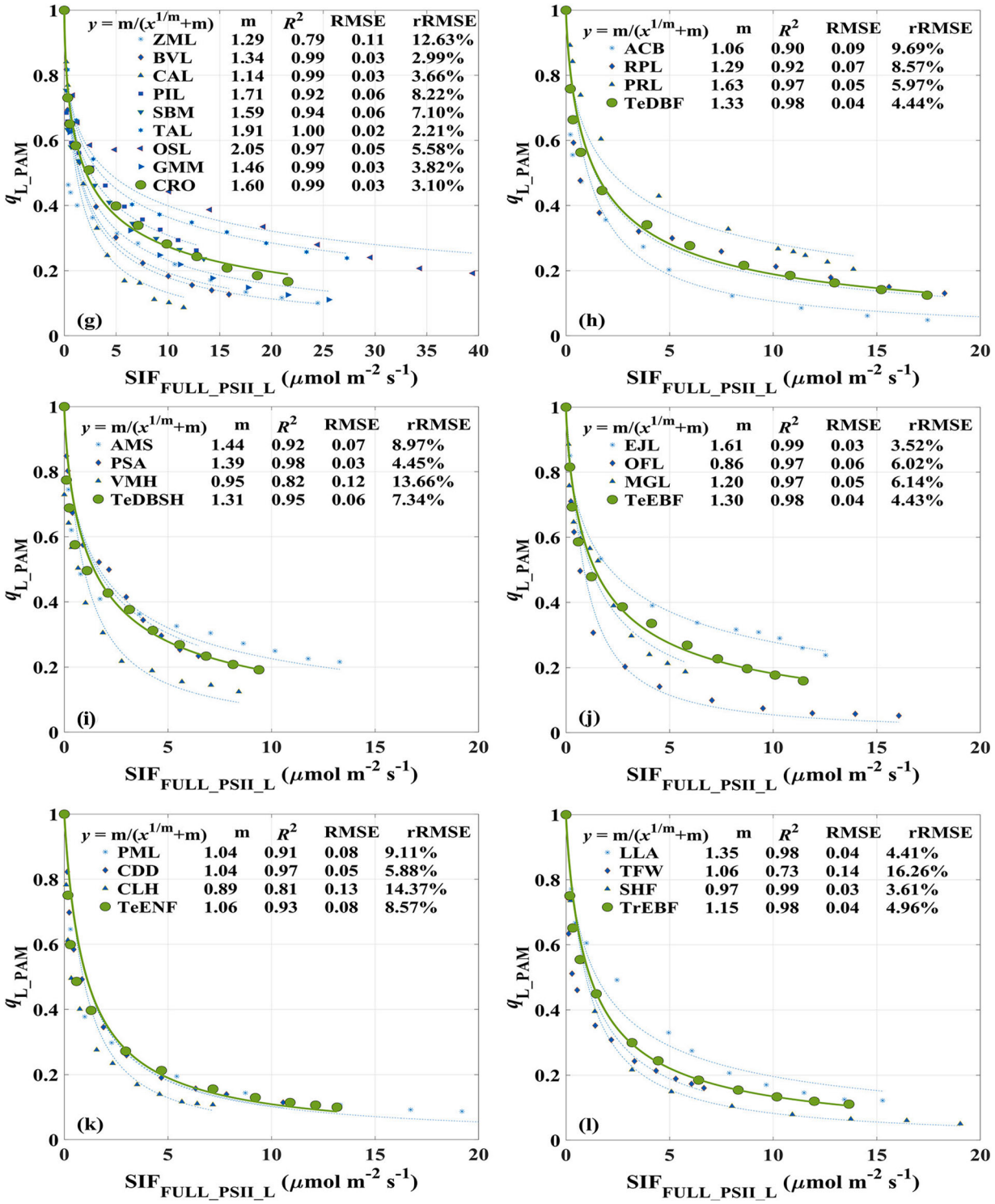

Fig. 5. (*continued*).

for 99% of the variance (C_3GRA with a root mean square error (RMSE) of 0.03 and a relative RMSE (rRMSE) of 3.09%, Fig. 5f; CRO with RMSE=0.03, rRMSE=3.10%, Fig. 5g). However, for BoDNF, the model's accuracy was lower, explaining only 90% of the variance (RMSE=0.09, rRMSE=10.23%, Fig. 5d). TeENF also had a relatively low explanatory power (RMSE=0.03, rRMSE=3.09%, Fig. 5k), with a correlation coefficient (R^2) of 0.93.

The explanatory power of the predictive q_L models also varied significantly among different species within the same PFT. In particular, for TrEBF there was a difference of up to 0.26 in R^2 values among species (Fig. 5l). In contrast, the BoDBF (Fig. 5b) and TeEBF (Fig. 5j) groups had minimal species differences (only a 0.02 difference). Among all 45 species, over half had models accounting for more than 95% of the variance, and only 11% had models with explanatory power below 90%, with *Trachycarpus fortunei* having the lowest accuracy ($R^2 = 0.73$, RMSE = 0.14, rRMSE = 16.26%, Fig. 5l).

The response of q_L to temperature generally followed a similar trend across different plant species, initially rising and then declining (Fig. 6,

Table S3). However, the magnitude of this response varies among PFTs. BoENF (Fig. 6e) had a weaker response, with q_{L_PAM} increasing by about 0.16 from its minimum at the optimal temperature. In contrast, TeDBSH (Fig. 6i) and TeEBF (Fig. 6j) exhibited stronger responses, with q_{L_PAM} increases exceeding 0.25. The other nine PFTs had moderate responses, with q_{L_PAM} increases around 0.2 at the optimal temperature. Arranged in order from weak to strong responses, these PFTs are: TrEBF (Fig. 6l), BoC$_3$GRA (Fig. 6a), BoDBSH (Fig. 6c), TeENF (Fig. 6k), BoDBF (Fig. 6b), TeDBF (Fig. 6h), C$_3$GRA (Fig. 6f), CRO (Fig. 6g), and BoDNF (Fig. 6d). The predictive q_L model effectively captured the temperature response, explaining 99% of the variance for the mean of all PFTs (Fig. 6).

We also calculated the leaf-scale q_L ($q_{L\_SIF\_L}$) based on $SIF_{FULL\_PSII\_L}$. Comparing $q_{L\_SIF\_L}$ to q_{L_PAM} across the entire dataset, which spans the full ranges of light intensity and leaf temperature across 12 PFTs, the proposed predictive q_L model, yielding $q_{L\_SIF\_L}$, explains 98% of the variance in the measured q_{L_PAM} (RMSE = 0.05, rRMSE = 5.46%), with

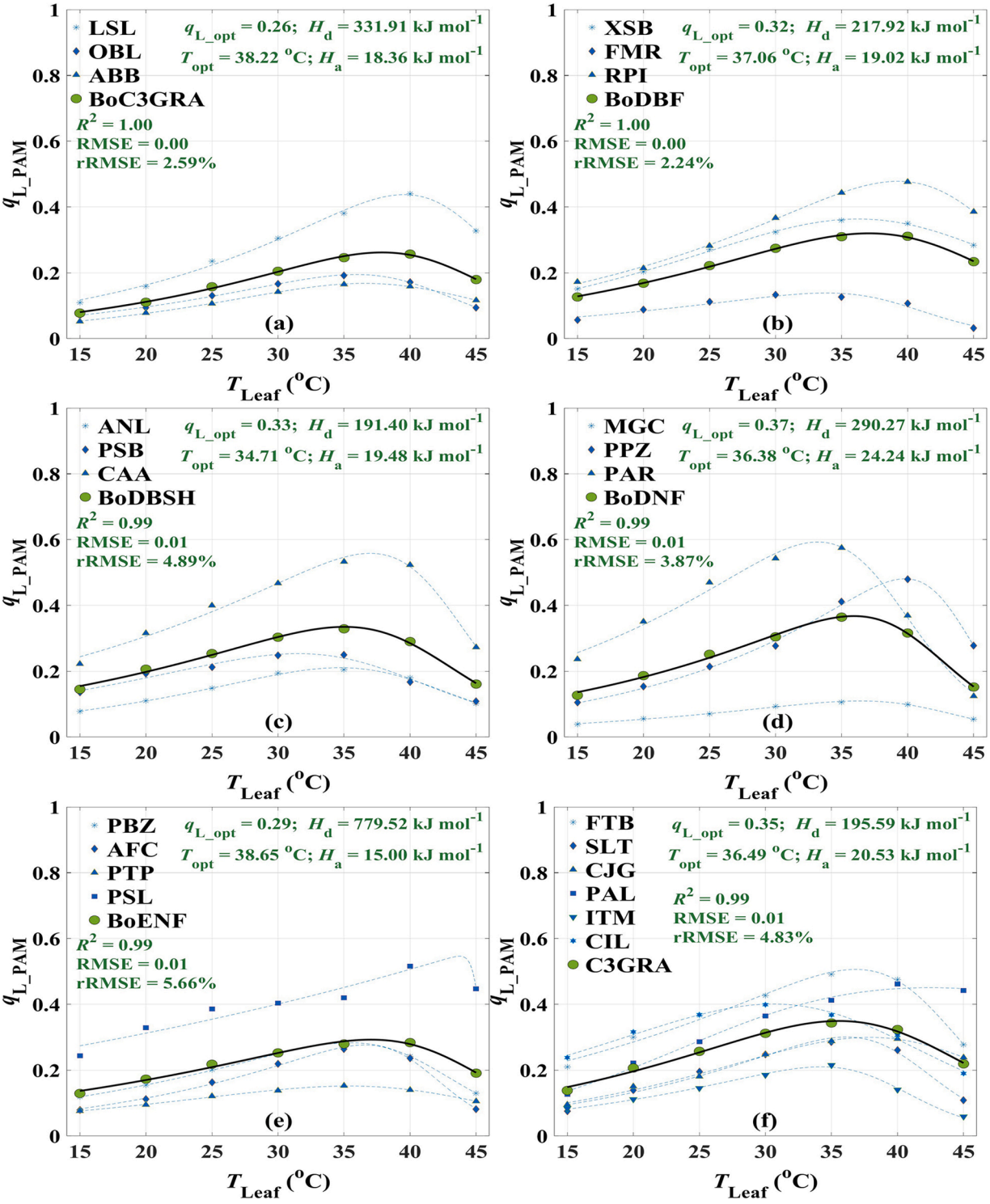

Fig. 6. The response curves of q_{L_PAM} to T_{leaf} derived from applying the proposed model under seven values of T_{leaf} for 45 plant species across 12 plant functional types (PFTs) (Table 1). The thin and bold curves represent individual species and the mean of all species, respectively, for each PFT. q_{L_PAM} is obtained from PSI fluorescence-corrected data measured with a PAM fluorometer; T_{leaf} is leaf temperature (°C).

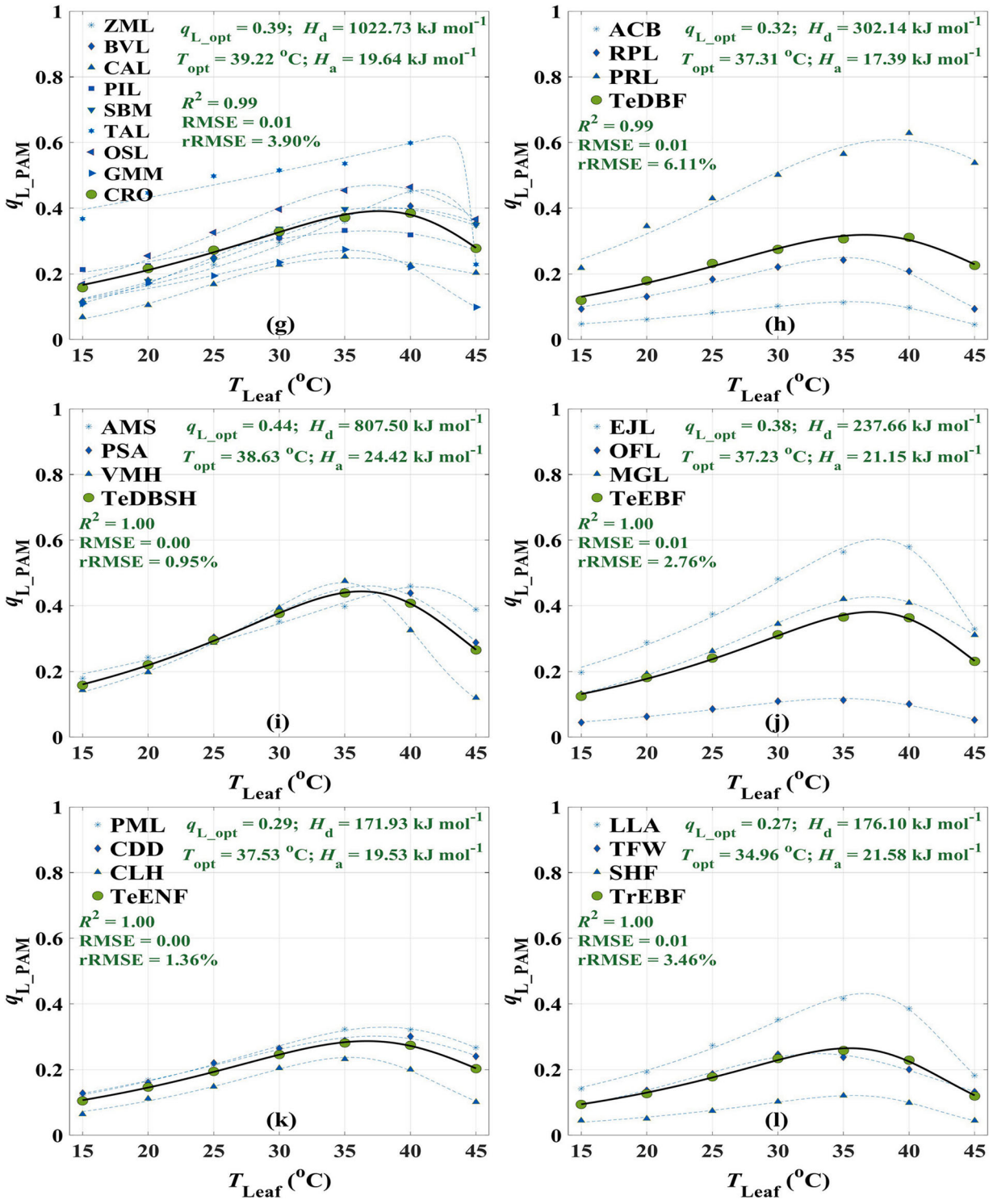

Fig. 6. (*continued*).

the regression closely aligning with the 1:1 line (Fig. S2). This high level of consistency confirms that our predictive q_L model can effectively simulate q_L across different species.

4.2. *The performance in estimating canopy-scale V_{cmax}*

Fig. 7 shows a comparison between V_{cmax_SIF} and V_{cmax_EC} at the daily scale across nine EC sites, highlighting significant differences in estimation accuracy among sites with different vegetation types. For all sites combined, the R^2 is 0.86, with a RMSE of 26.41 μmol m^{-2} s^{-1} and a rRMSE of 5.51% (Fig. S3). The highest estimation accuracy was achieved for the cropland sites. At the Gucheng and Yangling sites, V_{cmax_SIF} explained over 80% of the variability in the daily V_{cmax_EC} time series (Gucheng: RMSE = 31.31 μmol m^{-2} s^{-1}, rRMSE = 6.89%, Fig. 7b; Yangling: RMSE = 17.89 μmol m^{-2} s^{-1}, rRMSE = 11.71%, Fig. 7c). The Changling site also exhibited a strong correlation (R^2 = 0.71, RMSE = 32.07 μmol m^{-2} s^{-1}, rRMSE = 16.12%, Fig. 7a). Of the grassland sites, Panjin, representing temperate C_3 grasslands, had the highest

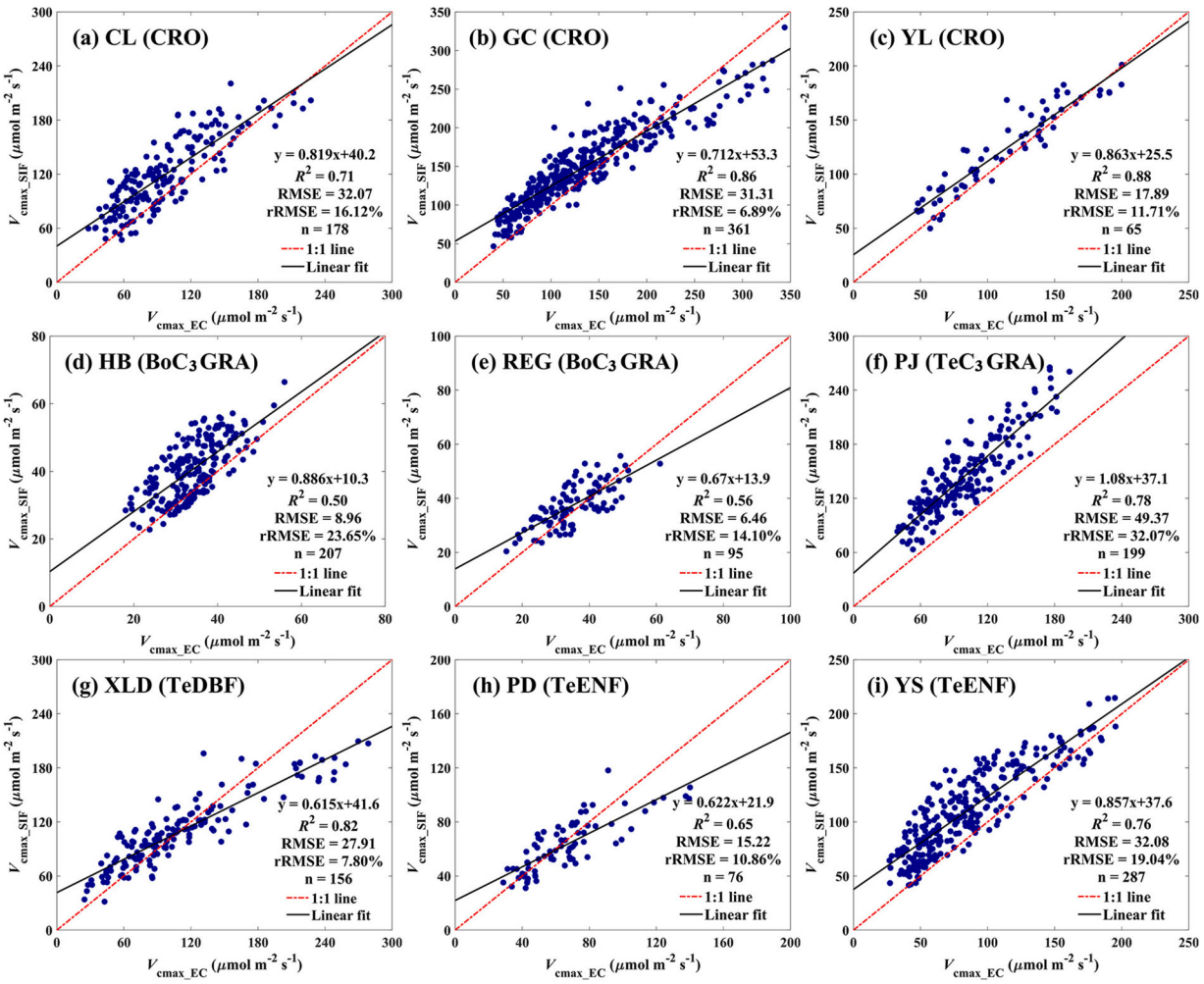

Fig. 7. Comparison between daily canopy-level V_{cmax} estimated from flux data and SIF observations (V_{cmax_EC} versus V_{cmax_SIF}, μmol m^{-2} s^{-1}) at nine eddy covariance flux sites (Table 2). The solid black lines indicate the linear regressions between the observed and predicted values. The 1:1 lines are shown by the red dashes.

estimation accuracy, with V_{cmax_SIF} explaining approximately 78% of the variance in V_{cmax_EC} (RMSE = 49.37 μmol m^{-2} s^{-1}, rRMSE = 32.07%, Fig. 7f). The estimates for the alpine meadow sites, Haibei and Ruoergai, had lower accuracies, explaining about 50% (RMSE = 8.96 μmol m^{-2} s^{-1}, rRMSE = 23.65%, Fig. 7d) and 56% (RMSE = 6.46 μmol m^{-2} s^{-1}, rRMSE = 14.10%, Fig. 7e) of the variance, respectively. Among the forest sites, Xiaolangdi, which is dominated by deciduous broadleaf forest, exhibited a high estimation accuracy, with V_{cmax_SIF} explaining over 80% of the variance in V_{cmax_EC} (RMSE = 27.91 μmol m^{-2} s^{-1}, rRMSE = 7.80%, Fig. 7g). Strong correlations were also observed at Puding (R^2 = 0.65, RMSE = 15.22 μmol m^{-2} s^{-1}, rRMSE = 10.86%, Fig. 7h) and Yanshan (R^2 = 0.76, RMSE = 32.08 μmol m^{-2} s^{-1}, rRMSE = 19.04%, Fig. 7i). We also compared V_{cmax_SIF} at 25 °C with V_{cmax_EC} at 25 °C at these sites (Fig. S4, Text S5). At 25 °C, there is a larger discrepancy between the SIF-based V_{cmax} and the EC-derived V_{cmax}, with the former explaining only approximately 69% of the variability in the latter (Fig. S5). This is primarily due to the significant influence of the empirical coefficient (i.e. E_{Vcmax}) when converting V_{cmax} to V_{cmax25}. The E_{Vcmax} can vary between 36,380 J mol^{-1} to 172,838 J mol^{-1} across different species.

Consistent with the site-level scatter comparisons, the daily V_{cmax} curves showed that the SIF-based estimates generally reproduced the temporal dynamics of EC-derived V_{cmax} at the selected flux tower sites. The agreement was particularly clear in cropland and forest ecosystems, although some differences in peak magnitude remained at several grassland sites (Fig. S6). We also summarized the multi-year mean daily V_{cmax_SIF} curves for the major plant functional types, which further highlighted clear cross-ecosystem differences in seasonal dynamics (Fig. S7). In particular, croplands exhibited the highest growing-season V_{cmax_SIF}, whereas boreal vegetation generally maintained lower values and weaker seasonal amplitudes.

4.3. Spatial–temporal variations in V_{cmax25}

We applied the proposed model to produce daily V_{cmax25} values over China's vegetated land surface for the period 2019–2022 (Fig. 8). Averaged over these years, the mean annual V_{cmax25} across areas with valid data was 87.25 μmol m^{-2} s^{-1} (Fig. 8, Table 3). Annual V_{cmax25} generally decreased from southeast to northwest China (Fig. 8), consistent with the broad hydrothermal gradient and vegetation distribution across the country. In the southeastern regions, characterized by warm, humid climates and abundant vegetation, higher V_{cmax25} values were observed. Conversely, the northwestern regions which are arid, cold, and have sparse vegetation exhibited lower V_{cmax25} values. Specifically, we identified three regions with high annual mean V_{cmax25} values (>120 μmol m^{-2} s^{-1}): the Sichuan Basin (Fig. 8, I), the Pearl River Delta (Fig. 8, II), and the middle and lower reaches of the Yangtze River (Fig. 8, III). In contrast, areas like the northern part of the Inner Mongolia Plateau (Fig. 8, IV) and regions such as Southeastern Tibetan Plateau (excluding the valley areas) (Fig. 8, V) and Xinjiang (Fig. 8, VI), where precipitation is less than 400 mm, generally had V_{cmax25} values below 60 μmol m^{-2} s^{-1} (Fig. 8). However, this broad southeast-to-

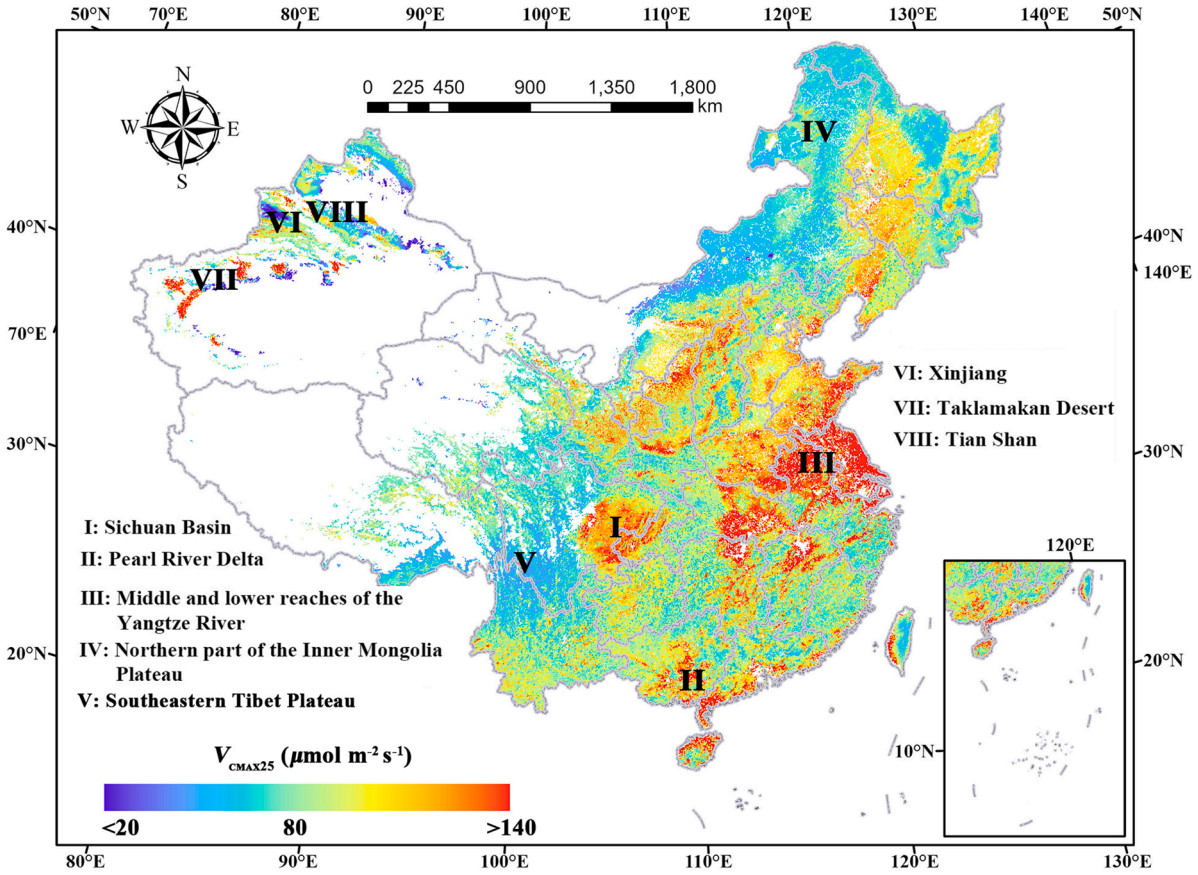

Fig. 8. Spatial distribution of mean annual ecosystem V_{cmax25} (μmol m^{-2} s^{-1}) estimated using the proposed model for 2019–2022, with a resolution of 0.05 degrees.

Table 3
Mean annual and seasonal V_{cmax25} (μmol m^{-2} s^{-1}) estimated from SIF observations across different plant functional types during 2019–2022. MAM, March–May; JJA, June–August; SON, September–November; DJF, December–February.

PFTs	Mean annual	MAM	JJA	SON	DJF
Boreal C_3 grass (BoC_3GRA)	64.05	54.06	61.77	54.58	48.32
Boreal deciduous broadleaf forest (BoDBF)	69.59	60.22	73.67	59.22	46.32
Boreal deciduous broadleaf shrub (BoDBSH)	63.00	54.84	66.47	54.38	42.77
Boreal deciduous needleleaf forest (BoDNF)	59.95	52.35	62.94	51.93	NAN
Boreal evergreen needleleaf forest (BoENF)	52.67	45.77	53.42	45.46	37.92
C_3 grass (C_3GRA)	69.97	61.84	77.80	58.83	51.35
Crops (CRO)	113.72	102.60	132.19	96.11	72.26
Temperate deciduous broadleaf forest (TeDBF)	86.07	75.52	99.26	73.49	59.00
Temperate deciduous broadleaf shrub (TeDBSH)	89.18	79.40	109.21	78.87	60.59
Temperate evergreen broadleaf forest (TeEBF)	79.00	70.14	100.93	72.45	53.28
Temperate evergreen needleleaf forest (TeENF)	62.66	54.94	78.69	57.47	41.61
Tropical evergreen broadleaf forest (TrEBF)	68.41	65.37	84.00	63.06	50.83
China	**87.25**	**77.01**	**99.97**	**74.03**	**54.84**

northwest gradient was locally modified by environmental and land-management factors. Relatively high V_{cmax25} values were observed in the oases at the edge of the Taklamakan Desert (Fig. 8, VII), where irrigation and groundwater availability can alleviate water limitation, and in the western Tian Shan (Fig. 8, VIII), where regional precipitation regimes influenced by Atlantic moisture provide more favorable water conditions (Fig. S8).

Ecosystem V_{cmax25} showed significant variation across different vegetation types (Table 3): croplands had the highest mean annual V_{cmax25} at 113.72 μmol m^{-2} s^{-1}, followed by temperate deciduous broadleaf shrub at 89.18 μmol m^{-2} s^{-1}, while boreal evergreen needleleaf forest showed the lowest values at 52.67 μmol m^{-2} s^{-1}. Given that the proposed model is designed to estimate C_3 photosynthetic capacity, the cropland estimates should primarily be interpreted within the framework of C_3 crop photosynthesis. The presence of C_4 crops, such as maize and sorghum, in some cropland regions may introduce additional uncertainty into the corresponding V_{cmax25} estimates. With the rapid rise in available energy and vegetation growth during summer, pronounced seasonality in V_{cmax25} was observed in croplands and temperate vegetation types (Fig. 9, Table 3). For instance, V_{cmax25} values in temperate deciduous broadleaf forest, temperate evergreen broadleaf forest, and temperate deciduous broadleaf shrub were much higher during the summer months (June, July, and August), increasing by more than 25 μmol m^{-2} s^{-1} from spring (March, April, and May) to summer. Conversely, by winter, the V_{cmax25} values dropped by around 15 μmol m^{-2} s^{-1} (Fig. 9, Table 3). In contrast, V_{cmax25} exhibited minimal seasonal variation in both boreal C_3 grasslands and tropical evergreen broadleaf forests, maintaining nearly the same values in each season (Fig. 9, Table 3).

Additional uncertainty and sensitivity analyses based on Sobol global sensitivity analysis and Monte Carlo uncertainty propagation further indicated that V_{cmax} uncertainty was primarily driven by a few dominant variables and parameters, among which f_w, K_{CO}, and m_{opt} were the three most influential factors, followed by SIF_{TOC_743} and $f_{esc\_P\text{-}C}$. The ranges of the variables and parameters used in these analyses are summarized in

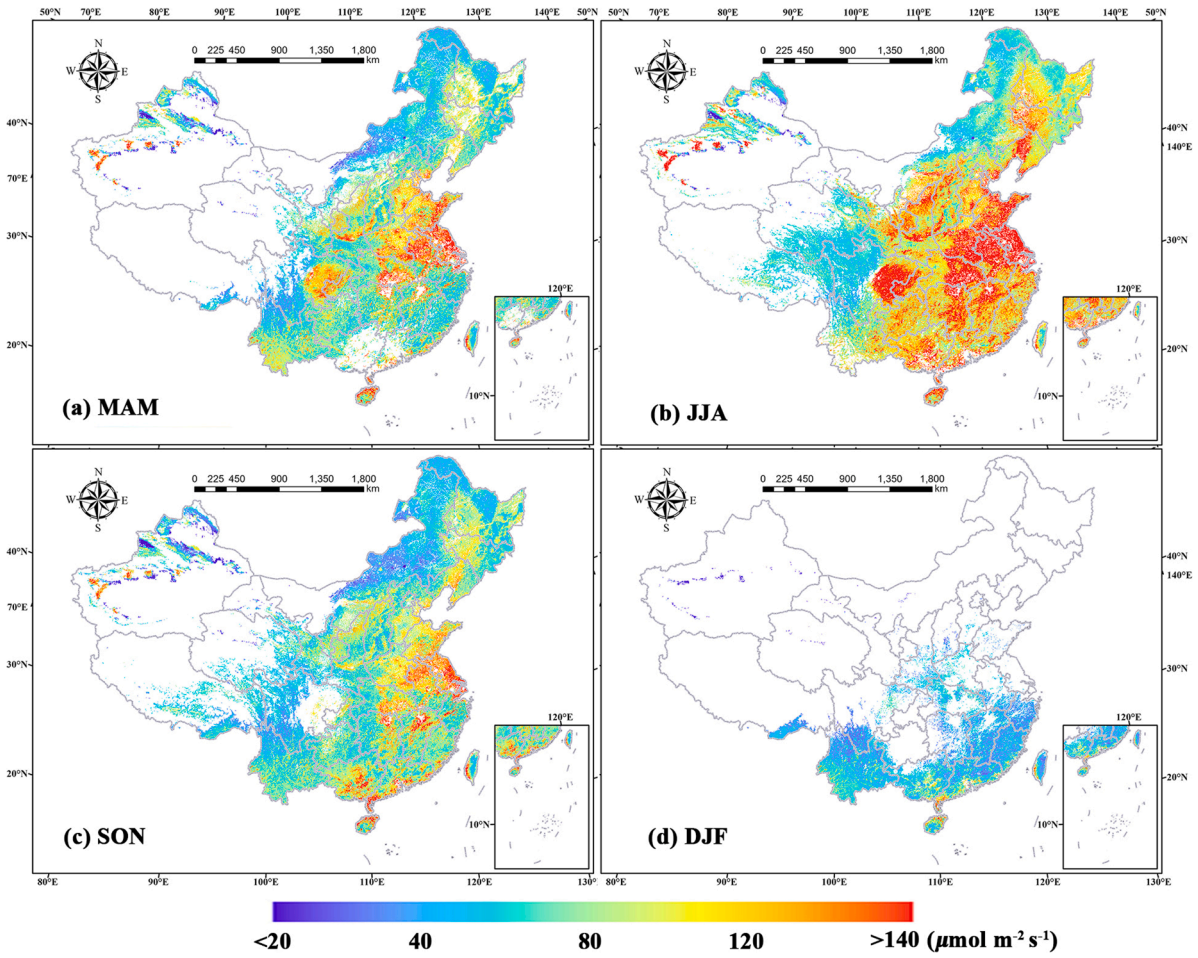

Fig. 9. The spatial patterns of the mean V_{cmax25} (μmol m^{-2} s^{-1}) estimated by the proposed model for spring (MAM, a), summer (JJA, b), autumn (SON, c) and winter (DJF, d) over the period 2019-2022.

Table S4. Uncertainty also differed among PFTs and generally declined from the daily to the monthly and annual scales, indicating that the broad spatiotemporal patterns described above were more robust when interpreted at coarser temporal resolutions (Figs. S9–S10).

At the spatial scale, we compared the V_{cmax25} estimated in this study (V_{cmax25_SIF}) with that derived from leaf chlorophyll content (LCC) data (V_{cmax25_LCC}, Luo et al., 2019). In Luo et al. (2019), a statistical relationship was established between a 500-m, 7-day temporal resolution LCC product (http://www.geodata.cn) and V_{cmax25}. We also compared our results with the growing season mean V_{cmax} (V_{cmaxTg}) obtained by Chen et al. (2022) using TROPOMI SIF and LCC data ($V_{cmaxTg\_SIF\_LCC}$). Chen et al. (2022) estimated growing-season V_{cmax} using a data assimilation framework that integrated TROPOMI SIF, LCC information, and an ecosystem model. In their framework, sunlit-leaf SIF was linked to GPP through a nonlinear SIF–GPP relationship, and LCC-derived V_{cmax} was used as an additional constraint to optimize the retrieval of V_{cmax} from SIF observations. They provided V_{cmax} at a 0.5° spatial resolution for the average growing season temperature in 2019. To ensure consistency, we applied a common temperature function (Eq. 22 in Smith et al., 2019) to convert the V_{cmax} estimated by our study into V_{cmaxTg} ($V_{cmaxTg\_SIF\_qL}$) for comparative analysis. And following the criterion established by Chen et al. (2022), we defined the growing season as the period when the monthly mean air temperature is above 0 °C.

Fig. 10a shows the spatial distribution of differences between V_{cmax25_LCC} and V_{cmax25_SIF} (where $\Delta V_{cmax25} = V_{cmax25\_LCC} - V_{cmax25\_SIF}$). Overall, there is a relatively large discrepancy between the two datasets: the mean V_{cmax25_LCC} for 2019 is 62.90 μmol m^{-2} s^{-1}, while our estimated V_{cmax25_SIF} is about 1.5 times higher, at 90.52 μmol m^{-2} s^{-1}. In approximately 80% (77.30%) of China's vegetated areas, V_{cmax25_SIF} has higher values compared to V_{cmax25_LCC}, leading to negative ΔV_{cmax25} values. The result showed that nearly 54.35% of the vegetated grid cells exhibit a ΔV_{cmax25} variation ranging from –30 to 30 μmol m^{-2} s^{-1} (Fig. 10a). These cells are primarily located in the Greater (Fig. 10a, I) and Lesser (Fig. 10a, II) Khingan Mountains and Changbai Mountain (Fig. 10a, III) in Northeast China and in the southeast region of China. In contrast, in region such as the Huang-Huai-Hai Plain (Fig. 10a, IV), the Sichuan Basin (Fig. 10a, V), and the oases at the edge of the Taklamakan Desert (Fig. 10a, VI), the ΔV_{cmax25} values are relatively low (< -50 μmol m^{-2} s^{-1}). A possible reason for this is that V_{cmax25_LCC} incorporates LCC information that tends to be converted to lower values of V_{cmax} using existing empirical relationships (Chen et al., 2022).

Fig. 10b further shows the corresponding relative percent difference in V_{cmax25}, calculated using V_{cmax25_SIF} as the reference. The spatial pattern of ΔV_{cmax25} (%) was generally consistent with that of the absolute difference shown in Fig. 10a. Negative values dominated most vegetated areas, accounting for approximately 78.31% of the valid pixels, indicating that V_{cmax25_LCC} was generally lower than V_{cmax25_SIF}. In particular, large negative relative differences were mainly observed in the Huang-Huai-Hai Plain (Fig. 10b, IV), the Sichuan Basin (Fig. 10b, V), and the oases at the edge of the Taklamakan Desert (Fig. 10b, VI), where the SIF-based estimates were substantially higher than the LCC-derived estimates. By contrast, relatively small differences or positive values were mainly found in parts of the Greater Khingan Mountains (Fig. 10b, I), Lesser Khingan Mountains (Fig. 10b, II), and Changbai Mountains (Fig. 10b, III). Overall, approximately 78.74% of the vegetated pixels showed relative differences within the range of −50% to 50%.

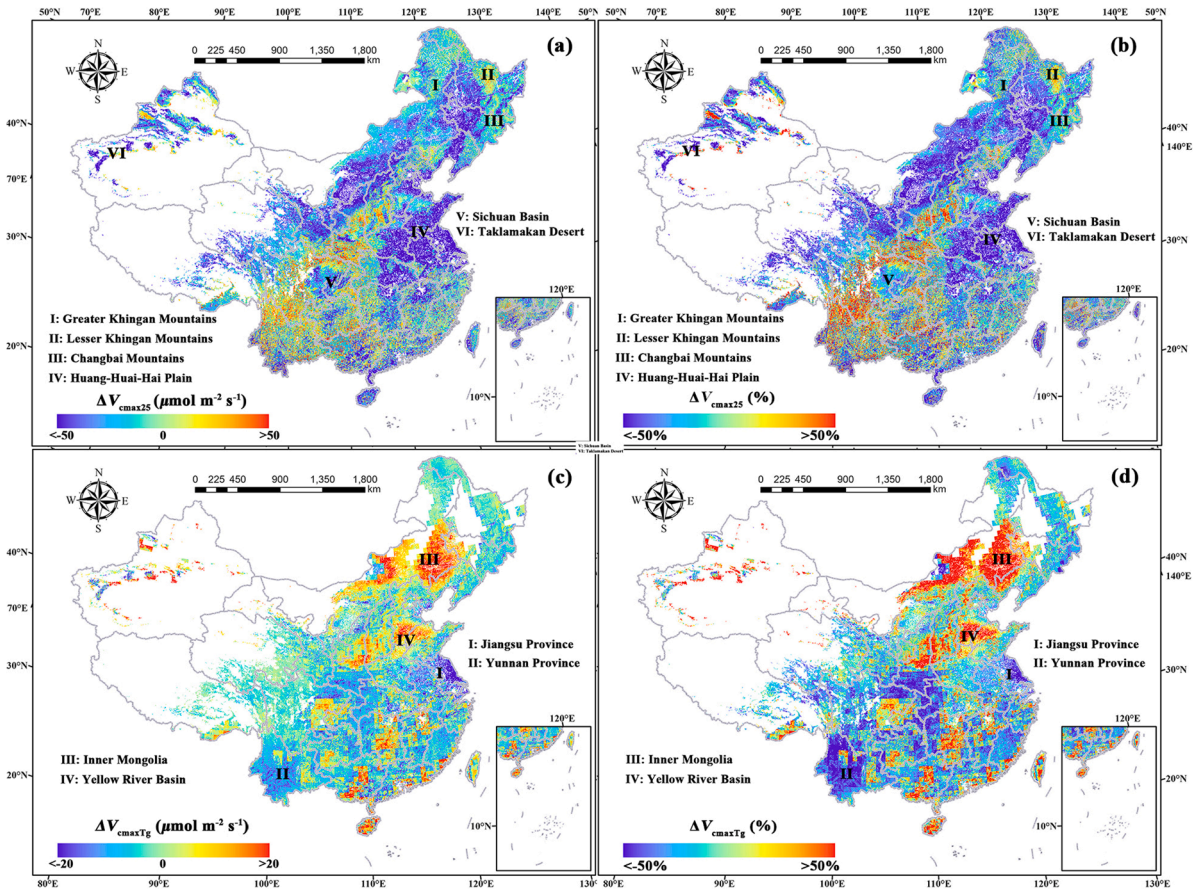

Fig. 10. Spatial comparisons between V_{cmax25} estimates from this study and existing products. (a): Spatial distribution of the absolute difference in V_{cmax25} between values obtained from LCC data (V_{cmax25_LCC}, μmol m^{-2} s^{-1}) and those from the proposed model (V_{cmax25_SIF}, μmol m^{-2} s^{-1}), calculated as $\Delta V_{cmax25} = V_{cmax25\_LCC}$ - V_{cmax25_SIF}. (b) Spatial distribution of the relative percent difference in V_{cmax25}, calculated as ΔV_{cmax25} (%) = (V_{cmax25_LCC} - V_{cmax25_SIF}) / V_{cmax25_SIF} × 100%. (c): Spatial distribution of the difference in growing season mean V_{cmaxTg} between values obtained from TROPOMI SIF and LCC data ($V_{cmaxTg\_SIF\_LCC}$, μmol m^{-2} s^{-1}) and those from the proposed model ($V_{cmaxTg\_SIF\_qL}$, μmol m^{-2} s^{-1}), calculated as $\Delta V_{cmaxTg} = V_{cmaxTg\_SIF\_LCC}$ - $V_{cmaxTg\_SIF\_qL}$. (d) Spatial distribution of the relative percent difference in V_{cmaxTg}, calculated as ΔV_{cmaxTg} (%) = ($V_{cmaxTg\_SIF\_LCC}$ - $V_{cmaxTg\_SIF\_qL}$) / $V_{cmaxTg\_SIF\_qL}$ × 100%.

Fig. 10c shows the spatial distribution of differences between $V_{cmaxTg\_SIF\_LCC}$ and $V_{cmaxTg\_SIF\_qL}$ (where $\Delta V_{cmaxTg} = V_{cmaxTg\_SIF\_LCC}$ - $V_{cmaxTg\_SIF\_qL}$). Overall, $V_{cmaxTg\_SIF\_qL}$ generally agrees well with $V_{cmaxTg\_SIF\_LCC}$: ΔV_{cmaxTg} varies in a small range between -10 and 10 μmol m^{-2} s^{-1} on 69.14% of the vegetated grid cells (Fig. 10c). In 64.14% of these vegetated areas, $V_{cmaxTg\_SIF\_qL}$ records higher values than $V_{cmaxTg\_SIF\_LCC}$, resulting in a negative ΔV_{cmaxTg}. The two hotspot regions are Jiangsu Province (Fig. 10c, I) and Yunnan Province (Fig. 10c, II). However, of these areas, only 18.21% have a ΔV_{cmaxTg} less than -10 μmol m^{-2} s^{-1} (Fig. 10c), indicating that the overestimation of the proposed model compared to the $V_{cmaxTg\_SIF\_LCC}$ estimation model is limited. Nearly 35% (35.86%) of China have a positive ΔV_{cmaxTg}, primarily distributed in the central and eastern regions of Inner Mongolia around 40°N (Fig. 10c, III) and parts of the middle and lower reaches of the Yellow River Basin (Fig. 10c, IV).

Fig. 10d presents the relative percent difference in V_{cmaxTg}, calculated using $V_{cmaxTg\_SIF\_qL}$ as the reference. Compared with the absolute difference map in Fig. 10c, the percent-difference map further highlights the proportional discrepancies between the two products. Positive ΔV_{cmaxTg} (%) values were mainly distributed in parts of northern and northeastern China, especially around Inner Mongolia (Fig. 10d, III) and the Yellow River Basin (Fig. 10d, IV), indicating that $V_{cmaxTg\_SIF\_LCC}$ was higher than $V_{cmaxTg\_SIF\_qL}$ in these regions. In contrast, negative relative differences were more evident in southern China, particularly around Jiangsu Province (Fig. 10d, I) and Yunnan Province (Fig. 10d, II), suggesting lower $V_{cmaxTg\_SIF\_LCC}$ relative to $V_{cmaxTg\_SIF\_qL}$. Overall, negative relative differences accounted for approximately 66.17% of the valid vegetated pixels, while approximately 83.48% of the pixels showed relative differences within −50% to 50%.

5. Discussion

Although GPP can be directly estimated from SIF using an MLR framework without explicitly incorporating V_{cmax}, this does not diminish the importance of estimating V_{cmax}. Beyond serving as a key input parameter in the FvCB model for GPP estimation, V_{cmax} carries broader ecological and physiological significance. Specifically, V_{cmax} represents the photosynthetic capacity of vegetation and reflects the long-term physiological acclimation of plants to environmental conditions over a given time scale, whereas GPP primarily captures an instantaneous state jointly regulated by environmental drivers such as radiation, temperature, and water availability. V_{cmax} can be interpreted as an expression of plant resource allocation and adaptive strategies, with its variation reflecting the regulation of trade-offs between light utilization and carbon acquisition under changing environmental conditions (Smith et al., 2019; Harrison et al., 2021; Prentice et al., 2014). Therefore, V_{cmax} should be viewed not merely as a model parameter, but as a key variable for understanding plant ecological strategies and climate adaptation processes-an aspect that cannot be replaced by approaches that directly estimate GPP from SIF. Furthermore, as a physiologically meaningful parameter, V_{cmax} can be readily integrated into process-based models, thereby enhancing their generality and predictive

capability. The SIF-based mechanistic estimation of V_{cmax} proposed in this study therefore provides an important contribution to advancing the quantitative characterization of vegetation photosynthetic mechanisms at the remote sensing scale.

Previous satellite approaches to estimate V_{cmax25} often rely on PFT-tuned proxies, on data-assimilation systems sensitive to the observation operator, or on mechanistic schemes that are difficult to scale; as a result, seasonality, within-PFT heterogeneity, or scalability may be compromised. This study presents a SIF-constrained canopy V_{cmax25} retrieval approach: first, within a SIF-q_L model, we used a leaf-level concurrent measurement system to calibrate parameters for 45 species spanning 12 major PFTs in China, yielding a cross-PFT parameterization of q_L; second, at the canopy scale (sunlit leaves) we established a diagnosis of Rubisco limitation, clarifying the applicability conditions of the SIF-based V_{cmax25} estimation model. Incorporating environmental constraints such as soil-moisture stress, we generated a China-wide V_{cmax25} dataset at 0.05° daily resolution for 2019–2022 and characterized the spatial and seasonal patterns across China's main PFTs, providing a scalable and mechanistically interpretable pathway for large-scale V_{cmax25} estimation.

It should be noted that C_4 plant photosynthetic carbon fixation is mainly limited by electron transport capacity (Gu et al., 2019), rather than V_{cmax}. Therefore, the model proposed in this paper is not suitable for estimating V_{cmax} in C_4 plants. For grassland ecosystems, the land-cover dataset used in this study only includes C_3 grass-related classes (Fig. 4); therefore, C_4 grassland regions were not considered in the estimation. However, the results over cropland regions dominated by C_4 crops (e.g., maize, sorghum) should be regarded as uncertain. There are some areas of our study which could be improved.

Although the leaf-level parameterization was based on measurements of 45 plant species across 12 major PFTs, the selected species may not fully represent the dominant species composition of each PFT across China. Therefore, the current parameterization should be regarded as a PFT-level functional approximation rather than a species-composition-weighted representation of each PFT. Additional variability may also arise when the PFT-level parameterization is applied across broad geographic regions, because regional climatic adaptation, long-term environmental acclimation, and differences in stand age may influence variables and parameters such as q_L, m_{opt}, T_{opt}, and $f_{PSII}(743)$. Future studies using multi-site observations with more regionally representative species across different climatic zones and stand development stages would help further evaluate and refine the parameterization framework.

Drought stress tends to reduce both $\Phi_{PSIImax}$ (Sommer et al., 2023) and q_L (Jia et al., 2023), or even K_{DF}, we assumed that $\Phi_{PSIImax}$ was a constant, and that the parameters used in the q_L estimation model were all derived from healthy, non-water-stressed leaves. We accounted for the effects of water stress on $\Phi_{PSIImax}$ and q_L by directly applying a water stress factor, f_w. In future research, a more in-depth analysis of the impact of water stress on V_{cmax} should be conducted, including how $\Phi_{PSIImax}$, q_L, and K_{DF} respond to water stress and avoiding the repetition of considering the impact of water stress. In particular, SIF combined with q_L can, in principle, track changes in the dark reactions of photosynthesis caused by stomatal closure due to water stress (Beauclaire et al., 2024; Han et al., 2022). In other words, a thorough analysis of how q_L and SIF vary in response to water stress may allow us to account for the impact of water stress on V_{cmax} more accurately.

In the derivation of V_{cmax25} from EC measurements, a crucial step involves using a rectangular hyperbola model to represent the photosynthetic light response curve (Wang et al., 2022a; Zheng et al., 2017). However, the performance of this semi-empirical model heavily depends on field measurements for calibrating its key parameters (Xie et al., 2018). Moreover, as an asymptotic line model, it has limitations in accurately depicting the actual photosynthetic light response curve-especially when light intensity exceeds the saturation point. Beyond this point, the actual photosynthetic rate decreases due to photoinhibition, a phenomenon that the rectangular hyperbola model fails to capture (Fang et al., 2015; Ye, 2010). This discrepancy between the model and observed data can lead to underestimation of the light saturation point and an overestimation of the maximum photosynthetic rate (Ye and Yu, 2008; Zhu et al., 2020). To address these limitations and enhance the model's accuracy, future research should focus on collecting more measured V_{cmax} data from flux stations to validate and improve its predictive capabilities. Additionally, alternative models–such as the modified rectangular hyperbola model–should be considered, as they may better fit the photosynthetic light response curve, particularly under low light and photoinhibition conditions (Ye and Yu, 2007; Ye and Yu, 2008) .

The SIF-based V_{cmax} model relies on $SIF_{SUN\_FULL\_PSII}$ as input, which depends on two key assumptions in Eqs. (5) – (7). First, we assume that the fluorescence yield ratio between sunlit and shaded leaves remains relatively constant across different vegetation types. Similarly, Yang et al. (2021) also found that sunlit leaves generally exhibit higher relative fluorescence emission efficiency than shaded leaves during the corn growth season, with both showing similar diurnal patterns. However, variations in leaf structure, chlorophyll content, and PSI/PSII chlorophyll ratios among vegetation types may challenge this assumption (Hogewoning et al., 2010; Kalaji et al., 2016). Furthermore, current PAM fluorometry cannot provide fluorescence yield in absolute units and relies on voltage signals to indirectly measure relative fluorescence yield, introducing additional uncertainty (Gu et al., 2019; Schreiber and Klughammer, 2021). These voltage signals are influenced by factors like chlorophyll content, the spectral properties of the measuring light, light intensity settings, amplifier gain, and detector filters, complicating direct comparisons across different devices or samples. In this study, we did not delve into the physiological differences between sunlit and shaded leaves. Instead, we used the SCOPE model to simplify these differences by comparing fluorescence yield ratios under varying light intensities. While this approach has inherent uncertainties, it offers a practical approximation given current technological limitation. The second assumption involves using a constant mean leaf-sun angle of 60°, which is a reasonable approximation for solar zenith angles between 30° and 60° (Chen et al., 1999). For solar zenith angles outside this range (<30° or >60°), the suitability of this constant requires further investigation. Achieving more accurate estimates of $APAR_{SUN}$ and $APAR_{SHA}$ would enhance the estimation of $SIF_{SUN\_FULL\_PSII}$.

6. Conclusion

In this study, we present a mechanistic model for estimating canopy V_{cmax} based on SIF, applicable when photosynthesis is Rubisco-limited. Using SIF emissions from sunlit leaves—derived from TOC SIF—with meteorological inputs, we were able to effectively estimate V_{cmax} (V_{cmax25}) at satellite overpass times across China from 2019 to 2022. Evaluations at nine sites showed that our model could reliably explain more than 80% of the variability across all vegetation types, with the best performance in croplands and the poorest in grasslands. Over this period, the mean annual V_{cmax25} over vegetated land surfaces in China was 87.25 $\mu mol\ m^{-2}\ s^{-1}$, underscoring the strong spatiotemporal variation in V_{cmax25}. This work demonstrates the effectiveness of large-scale applications based on satellite data and mechanistic methods, revealing critical spatial information about V_{cmax25}—such as in oasis croplands—and further unlocks the potential of SIF in modeling V_{cmax25}.

CRediT authorship contribution statement

Jingjing Yang: Conceptualization, Data curation, Methodology, Writing – original draft. **Zhunqiao Liu:** Funding acquisition, Investigation, Methodology, Writing – review & editing. **Chenhui Guo:** Conceptualization, Data curation, Investigation, Methodology, Writing – review & editing. **Qiang Yu:** Resources. **Shiwen Wang:** Validation. **Xiaoliang Lu:** Conceptualization, Funding acquisition, Methodology, Project administration, Supervision, Writing – review & editing.

Declaration of competing interest

The authors declare that they have no known competing financial interests or personal relationships that could have appeared to influence the work reported in this paper.

Acknowledgments

The research was supported by the National Natural Science Foundation of China (Grant No. 42471420 to Z.L., 42071328 to X.L., 42501482 to J.Y), the Chinese Universities Scientific Fund (24520212452021125 to X.L.), the Postdoctoral Fellowship Program of CPSF (GZC20251680 to J.Y) and the Shaanxi Province Postdoctoral Science Foundation (2024BSHYDZZ015 to J.Y) We thank the Exhibition Garden at Northwest A&F University for the experimental support provided.

Supplementary materials

Supplementary material associated with this article can be found, in the online version, at doi:10.1016/j.agrformet.2026.111370.

Appendix A. Definitions of symbols and units used.

Symbols	Definition	Unit
α	Mean leaf-sun angle	°
α_L	Leaf scattering coefficient	\
A_c	The Rubisco limited rate of CO_2 assimilation	μmol m^{-2} s^{-1}
A_j	The electron transport limited rate of CO_2 assimilation	μmol m^{-2} s^{-1}
$APAR_{SUN}$	The absorbed PAR for sunlit leaves	μmol m^{-2} s^{-1}
$APAR_{SHA}$	The absorbed PAR for shaded leaves	μmol m^{-2} s^{-1}
β_2	The fraction of APAR that is received by PSII	\
C	The multiple scattering of direct radiation	μmol m^{-2} s^{-1}
C_a	Ambient CO_2 partial pressure	μmol mol^{-1}
C_i	Chloroplastic CO_2 partial pressure	μbar
CI	Clumping index	\
δ	Constant value	$\mu$$mol^{-1}$ m^2 s
D_{Jmax}	The energies of deactivation	J mol^{-1}
E_{Jmax}	The energies of activation	J mol^{-1}
E_{Vcmax}	The activation energy	J mol^{-1}
E_{Kc}	Activation energy	J mol^{-1}
E_{Ko}	Activation energy	J mol^{-1}
f_{PSII}	The relative contribution of PSII fluorescence to total fluorescence	\
f_{APAR}	The fraction of absorbed PAR	\
$f_C(\lambda)$	The ratio for converting $SIF_{TOT\_760\_PSII}$ to $SIF_{TOT\_\lambda\_PSII}$ for a specific wavelength λ ($640 \leq \lambda \leq 850$ nm)	\
$f_{esc\_P\text{-}C}$	The fraction of SIF photons escaping from the PSII reaction centers to TOC.	\
f_w	Empirical function of soil moisture variation	\
F_m	Maximal fluorescence yields	\
F_m'	Light-adapted maximal fluorescence yield	\
F_o	Minimal fluorescence yields	\
F_o'	The minimum fluorescence yield in light-adapted state	\
F_s	Steady-state active fluorescence yield	\
g_1	Fitting parameter related to the plant's water use strategy	$kPa^{0.5}$
H_a	The rate at which the peak function increases below T_{opt}	(kJ mol^{-1})
H_d	The rate at which the peak function decreases above T_{opt}	(kJ mol^{-1})
i_0	Canopy interceptance	\
J	The electron transport rate	μmol m^{-2} s^{-1}
J_{max}	The maximum electron transport rate	μmol m^{-2} s^{-1}
J_{max25}	J_{max} at a standard temperature	μmol m^{-2} s^{-1}
K_c	The temperature dependent Rubisco Michaelis-Menten constants for CO_2	mol mol^{-1}
K_{c25}	The Michaelis-Menten constant for CO_2 at 25°C	mol mol^{-1}
K_{CO}	Composite parameter for Michaelis–Menten constants for RuBP carboxylation and oxygenation	μbar
K_{DF}	The ratio of K_D to K_F	\
K_o	The temperature dependent Rubisco Michaelis-Menten constants for O_2	mol mol^{-1}
K_{o25}	The Michaelis-Menten constant for O_2 at 25°C	mol mol^{-1}
LAI	Total leaf area index	m^2 m^{-2}
LAI_{SUN}	LAI for sunlit leaves	m^2 m^{-2}
LAI_{SHA}	LAI for shaded leaves	m^2 m^{-2}
λ	Wavelength	nm
m	The fitted parameter for estimating q_{L_SIF}	\
m_{opt}	The value of m at T_{opt}	\
O	Oxygen partial pressure	mol mol^{-1}
P	The probability of PAR_{DIF} being absorbed by sunlit leaves inside the canopy	\
PAR	Incoming photosynthetically active radiation	μmol m^{-2} s^{-1}
PAR_{DIF}	The diffuse component of PAR	\
PAR_{DIF_UNDER}	The portion of diffuse PAR under the plant canopy	\
PAR_{DIR}	The direct component of PAR	\
PAR_{SUN}	PAR for sunlit leaves	μmol m^{-2} s^{-1}
PAR_{SHA}	PAR for shaded leaves	μmol m^{-2} s^{-1}
q_L	The fraction of open Photosystem II reaction centers	\

(continued on next page)

(*continued*)

Symbols	Definition	Unit
q_{L_SUN}	q_L for sunlit leaves	\
q_{L_PAM}	Leaf-level q_L derived from PSI fluorescence-corrected data measured by a PAM fluorometer	\
R_{gas}	The molar gas constant	m^3 Pa mol^{-1} K^{-1}
R_λ	Reflectance of leaf	\
R_{veg}	Vegetation far-red reflectance	\
$SIF_{SUN\_FULL\_PSII}$	The broadband SIF flux density from sunlit leaves	μmol m^{-2} s^{-1}
$SIF_{SHA\_FULL\_PSII}$	The broadband SIF flux density from shaded leaves	μmol m^{-2} s^{-1}
SIF_{TOC_λ}	Top-of-canopy (TOC) SIF observations at a given wavelength, λ	mW m^{-2} nm^{-1} sr^{-1}
$SIF_{TOT\_FULL\_PSII}$	The broadband total PSII SIF flux density, where the subscript TOT refers to all leaves in the canopy	μmol m^{-2} s^{-1}
$SIF_{FULL\_PSII\_L}$	The full-band SIF radiation emitted from Photosystem II (PSII), where the subscript L refers to leaves	μmol m^{-2} s^{-1}
SIF_{up_λ}	Upwelling spectral fluorescence radiance at the leaf level	mW m^{-2} nm^{-1} sr^{-1}
SIF_{down_λ}	Downwelling spectral fluorescence radiance at the leaf level	mW m^{-2} nm^{-1} sr^{-1}
S_{Jmax}	The entropy term	J K^{-1} mol^{-1}
SZA	Solar zenith angle	◦
θ_S	The measured root-zone soil water content	m^3 m^{-3}
θ_W	SWC at wilting point	\
θ_F	SWC at field capacity	\
θ	Daily mean solar zenith angle	◦
θ_I	The relative contribution of PSI fluorescence to total fluorescence emission at the F_o level	\
θ_J	An empirical curvature parameter	\
σ	The product of $\Phi_{PSIImax}$, leaf light absorptance and fraction of absorbed photons allocated to PSII	\
T_{air}	Canopy air temperature	K
T_{Leaf}	Leaf temperature	K
T_{opt}	The optimal temperature for T_{Leaf}	K
T_λ	Transmittance of leaf	\
Γ^*	Chloroplastic compensation point of CO_2	μbar
V_{cmax}	The maximum carboxylation rate	μmol·m^{-2}·s^{-1}
V_{cmax25}	V_{cmax} at 25°C	μmol·m^{-2}·s^{-1}
V_{cmax25_EC}	Canopy-level V_{cmax25} estimated from EC measurements	μmol·m^{-2}·s^{-1}
V_{cmax25_SIF}	Canopy-level V_{cmax25} estimated from the proposed model	μmol·m^{-2}·s^{-1}
V_{cmax25_LCC}	Canopy-level V_{cmax25} obtained from LCC data	μmol·m^{-2}·s^{-1}
V_{cmaxTg}	V_{cmax} at the mean growing temperature	μmol·m^{-2}·s^{-1}
$V_{cmaxTg\_SIF\_LCC}$	V_{cmaxTg} obtained from TROPOMI SIF and LCC data	μmol·m^{-2}·s^{-1}
$V_{cmaxTg\_SIF\_qL}$	V_{cmaxTg} obtained from the proposed model	μmol·m^{-2}·s^{-1}
VPD	Vapor pressure deficit	kPa
w	Leaf albedo	\
$\Phi_{PSIImax}$	The maximum photochemical quantum yield of PSII under unstressed conditions	\
$\Phi_{SUN\_SIF\_PSII}$	The quantum yield of PSII SIF emission of sunlit leaves	\
$\Phi_{SHA\_SIF\_PSII}$	The quantum yield of PSII SIF emission of shaded leaves	\

Data availability

The data used for the analyses are available at . https://github.com/luxiaoliangnwafu/Dataset-multiSpecies

References

Alton, P.B., 2018. Decadal trends in photosynthetic capacity and leaf area index inferred from satellite remote sensing for global vegetation types. Agric. For. Meteorol 250-251, 361–375.

Bacour, C., Maignan, F., Macbean, N., Porcar-Castell, A., Flexas, J., Frankenberg, C., Peylin, P., Chevallier, F., Vuichard, N., Bastrikov, V., 2019. Improving estimates of gross primary productivity by assimilating solar-induced fluorescence satellite retrievals in a terrestrial biosphere model using a process-based SIF model. J. Geophys. Res. Biogeosci. 124, 3281–3306.

Beauclaire, Q., De Cannière, S., Jonard, F., Pezzetti, N., Delhez, L., Longdoz, B., 2024. Modeling gross primary production and transpiration from sun-induced chlorophyll fluorescence using a mechanistic light-response approach. Remote Sens. Environ. 307, 114150.

Bernacchi, C.J., Singsaas, E.L., Pimentel, C., Portis, A.R., Long, S.P., 2001. Improved temperature response functions for models of Rubisco-limited photosynthesis. Plant. Cell. Environ. 24, 253–259.

Bu, J., Gan, G., Chen, J., Su, Y., Yuan, M., Gao, Y., Domingo, F., López-Ballesteros, A., Migliavacca, M., El-Madany, T.S., Gentine, P., Xiao, J., Garcia, M., 2024. Dryland evapotranspiration from remote sensing solar-induced chlorophyll fluorescence: Constraining an optimal stomatal model within a two-source energy balance model. Remote Sens. Environ. 303, 113999.

Chen, J.M., Liu, J., Cihlar, J., Goulden, M.L., 1999. Daily canopy photosynthesis model through temporal and spatial scaling for remote sensing applications. Ecol. Modell. 124, 99–119.

Chen, J.M., Wang, R., Liu, Y., He, L., Croft, H., Luo, X., Wang, H., Smith, N.G., Keenan, T. F., Prentice, I.C., Zhang, Y., Ju, W., Dong, N., 2022. Global datasets of leaf photosynthetic capacity for ecological and earth system research. Earth Syst. Sci. Data 14, 4077–4093.

Croft, H., Chen, J.M., Luo, X., Bartlett, P., Chen, B., Staebler, R.M., 2017. Leaf chlorophyll content as a proxy for leaf photosynthetic capacity. Glob. Chang. Biol. 23, 3513–3524.

Cui, T., Sun, R., Xiao, Z., Liang, Z., Wang, J., 2020. Simulating spatially distributed solar-induced chlorophyll fluorescence using a BEPS-SCOPE coupling framework. Agric. For. Meteorol. 295, 108169.

Fang, L., Zhang, S., Zhang, G., Liu, X., Xia, X., Zhang, S., Xing, W., Fang, X., 2015. Application of five light-response models in the photosynthesis of Populus × Euramericana cv. 'Zhonglin46' Leaves. Appl. Biochem. Biotechnol. 176, 86–100.

Farquhar, G.D., Von Caemmerer, S., Berry, J.A., 1980. A biochemical model of photosynthetic CO2 assimilation in leaves of C3 species. Planta 149, 78–90.

Galmés, J., Medrano, H., Flexas, J., 2007. Photosynthetic limitations in response to water stress and recovery in Mediterranean plants with different growth forms. New Phytol. 175, 81–93.

Gu, L., Han, J., Wood, J.D., Chang, C.Y.Y., Sun, Y., 2019. Sun-induced Chl fluorescence and its importance for biophysical modeling of photosynthesis based on light reactions. New Phytol. 223, 1179–1191.

Guanter, L., Bacour, C., Schneider, A., Aben, I., Van Kempen, T.A., Maignan, F., Retscher, C., Köhler, P., Frankenberg, C., Joiner, J., Zhang, Y., 2021. The TROPOSIF global sun-induced fluorescence dataset from the Sentinel-5P TROPOMI mission. Earth Syst. Sci. Data 13, 5423–5440.

Guo, C., Liu, Z., Jin, X., Lu, X., 2024. Improved estimation of gross primary productivity (GPP) using solar-induced chlorophyll fluorescence (SIF) from photosystem II. Agric. For. Meteorol. 354, 110090.

Guo, Y., Zeng, J., Wu, W., Hu, S., Liu, G., Wu, L., Bryant, C.R., 2021. Spatial and temporal changes in vegetation in the Ruoergai Region, China. Forests 12, 76.

Han, J., Gu, L., Wen, J., Sun, Y., 2022. Inference of photosynthetic capacity parameters from chlorophyll a fluorescence is affected by redox state of PSII reaction centers. Plant. Cell. Environ. 45, 1298–1314.

Harley, P., Thomas, R., Reynolds, J., Strain, B.J.P., 1992. Modelling photosynthesis of cotton grown in elevated CO2. Cell, Environ. 15, 271–282.

Harrison, S.P., Cramer, W., Franklin, O., Prentice, I.C., Wang, H., Brännström, Å., de Boer, H., Dieckmann, U., Joshi, J., Keenan, T.F., Lavergne, A., Manzoni, S., Mengoli, G., Morfopoulos, C., Peñuelas, J., Pietsch, S., Rebel, K.T., Ryu, Y., Smith, N.

G., Stocker, B.D., Wright, I.J., 2021. Eco-evolutionary optimality as a means to improve vegetation and land-surface models. New Phytol. 231, 2125–2141.
He, L., Chen, J.M., Liu, J., Zheng, T., Wang, R., Joiner, J., Chou, S., Chen, B., Liu, Y., Liu, R., Rogers, C., 2019. Diverse photosynthetic capacity of global ecosystems mapped by satellite chlorophyll fluorescence measurements. Remote Sens. Environ. 232, 111344.
He, L., Chen, J.M., Pisek, J., Schaaf, C.B., Strahler, A.H., 2012. Global clumping index map derived from the MODIS BRDF product. Remote Sens. Environ. 119, 118–130.
He, M., Ju, W., Zhou, Y., Chen, J., He, H., Wang, S., Wang, H., Guan, D., Yan, J., Li, Y., Hao, Y., Zhao, F., 2013. Development of a two-leaf light use efficiency model for improving the calculation of terrestrial gross primary productivity. Agric. For. Meteorol. 173, 28–39.
He, Y., Wang, L., Niu, Z., Nath, B., 2022. Vegetation recovery and recent degradation in different karst landforms of southwest China over the past two decades using GEE satellite archives. Ecol. Inform. 68.
Hogewoning, S.W., Douwstra, P., Trouwborst, G., Van Ieperen, W., Harbinson, J., 2010. An artificial solar spectrum substantially alters plant development compared with usual climate room irradiance spectra. J. Exp. Bot. 61, 1267–1276.
Huang, J., Yue, X., Wang, B., Lu, X., Dong, G., 2024. Impact of diffuse radiation on the coupling of carbon and water fluxes in the grassland of northeastern China. Environ. Res. Lett. 19.
Jia, Q., Liu, Z., Guo, C., Wang, Y., Yang, J., Yu, Q., Wang, J., Zheng, F., Lu, X., 2023. Relationship between Photosynthetic CO2 Assimilation and Chlorophyll Fluorescence for Winter Wheat under Water Stress. Plants 12, 3365.
Kalaji, H.M., Schansker, G., Brestic, M., Bussotti, F., Calatayud, A., Ferroni, L., Goltsev, V., Guidi, L., Jajoo, A., Li, P., Losciale, P., Mishra, V.K., Misra, A.N., Nebauer, S.G., Pancaldi, S., Penella, C., Pollastrini, M., Suresh, K., Tambussi, E., Yanniccari, M., Zivcak, M., Cetner, M.D., Samborska, I.A., Stirbet, A., Olsovska, K., Kunderlikova, K., Shelonzek, H., Rusinowski, S., Bąba, W., 2016. Frequently asked questions about chlorophyll fluorescence, the sequel. Photosynth. Res 132, 13–66.
Kattge, J., Knorr, W., 2007. Temperature acclimation in a biochemical model of photosynthesis: a reanalysis of data from 36 species. Plant. Cell. Environ. 30, 1176–1190.
Köhler, P., Frankenberg, C., Magney, T.S., Guanter, L., Joiner, J., Landgraf, J., 2018. Global retrievals of solar induced chlorophyll fluorescence with TROPOMI: first results and inter-sensor comparison to OCO-2. Geophys. Res. Lett. 45, 10456–10463.
Liu, Y., Chen, J.M., He, L., Wang, R., Smith, N.G., Keenan, T.F., Rogers, C., Li, W., Leng, J., 2023. Global photosynthetic capacity of C3 biomes retrieved from solar-induced chlorophyll fluorescence and leaf chlorophyll content. Remote Sens. Environ. 287, 113457.
Liu, Y., Chen, J.M., Xu, M., Wang, R., Fan, W., Li, W., Kammer, L., Prentice, C., Keenan, T.F., Smith, N.G, 2024a. Improved global estimation of seasonal variations in C3 photosynthetic capacity based on eco-evolutionary optimality hypotheses and remote sensing. Remote Sens. Environ. 313, 114338.
Liu, Z., Guo, C., Yu, Q., Zhu, P., Peng, X., Dong, M., Cai, H., Lu, X., 2024b. A SIF-based approach for quantifying canopy photosynthesis by simulating the fraction of open PSII reaction centers (qL). Remote Sens. Environ. 305, 114111.
Liu, Z., Zhao, F., Liu, X., Yu, Q., Wang, Y., Peng, X., Cai, H., Lu, X., 2022. Direct estimation of photosynthetic CO2 assimilation from solar-induced chlorophyll fluorescence (SIF). Remote Sens. Environ. 271, 112893.
Long, S.P., Postl, W.F., Bolharnordenkampf, H.R., 1993. Quantum yields for uptake of carbon dioxide in C3 vascular plants of contrasting habitats and taxonomic groupings. Planta 189, 226–234.
Luo, X., Croft, H., Chen, J.M., He, L., Keenan, T.F., 2019. Improved estimates of global terrestrial photosynthesis using information on leaf chlorophyll content. Glob. Chang. Biol 25, 2499–2514.
Ma, Z., Xu, J., Ma, Y., Zhu, S., He, K., Zhang, S., Ma, W., Xu, X., 2022. AERA5-Asia: A long-term asian precipitation dataset (0.1°, 1-hourly, 1951–2015, Asia) anchoring the ERA5-land under the total volume control by APHRODITE. Bull. Amer. Meteor. Soc. 103, E1146–E1171.
Medlyn, B.E., Dreyer, E., Ellsworth, D., Forstreuter, M., Harley, P.C., Kirschbaum, M.U.F., Le Roux, X., Montpied, P., Strassemeyer, J., Walcroft, A., Wang, K., Loustau, D., 2002. Temperature response of parameters of a biochemically based model of photosynthesis. I. A review of experimental data. Plant. Cell. Environ. 25, 1167–1179.
Montzka, C., Herbst, M., Weihermüller, L., Verhoef, A., Vereecken, H., 2017. A global data set of soil hydraulic properties and sub-grid variability of soil water retention and hydraulic conductivity curves. Earth Syst. Sci. Data 9, 529–543.
Muñoz-Sabater, J., Dutra, E., Agustí-Panareda, A., Albergel, C., Arduini, G., Balsamo, G., Boussetta, S., Choulga, M., Harrigan, S., Hersbach, H., Martens, B., Miralles, D.G., Piles, M., Rodríguez-Fernández, N.J., Zsoter, E., Buontempo, C., Thépaut, J.-N., 2021. ERA5-Land: a state-of-the-art global reanalysis dataset for land applications. Earth Syst. Sci. Data 13, 4349–4383.
Myneni, R., Knyazikhin, Y., Park, T., 2021. MODIS/Terra+Aqua Leaf Area Index/FPAR 4-Day L4 Global 500m SIN Grid V061 [Data set]. NASA LP DAAC.
Prentice, I.C., Dong, N., Gleason, S.M., Maire, V., Wright, I.J., 2014. Balancing the costs of carbon gain and water transport: testing a new theoretical framework for plant functional ecology. Ecol. Lett. 17, 82–91.
Ran, Y.H., Li, X., Lu, L., Li, Z.Y., 2012. Large-scale land cover mapping with the integration of multi-source information based on the Dempster–Shafer theory. Int. J. Geogr. Inf. Sci. 26, 169–191.
Schreiber, U., Klughammer, C., 2021. Evidence for variable chlorophyll fluorescence of photosystem I in vivo. Photosynth. Res. 149, 213–231.
Smith, N.G., Keenan, T.F., Prentice, Colin, Wang, I., Wright, H., I, J., Niinemets, Ü., Crous, K.Y., Domingues, T.F., Guerrieri, R., Ishida, Yoko, Kattge, F., Kruger, J., E, L., Maire, V., Rogers, A., Serbin, S.P., Tarvainen, L., Togashi, H.F., Townsend, P.A., Wang, M., Weerasinghe, L.K., Zhou, S.X., Niu, S., 2019. Global photosynthetic capacity is optimized to the environment. Ecol. Lett. 22, 506–517.
Sommer, S.G., Han, E., Li, X., Rosenqvist, E., Liu, F., 2023. The chlorophyll fluorescence parameter fv/fm correlates with loss of grain yield after severe drought in three wheat genotypes grown at two CO2 concentrations. Plants 12, 436.
Tong, X., Mu, Y., Zhang, J., Meng, P., Li, J., 2019. Water stress controls on carbon flux and water use efficiency in a warm-temperate mixed plantation. J. Hydrol. 571, 669–678.
Van Der Tol, C., Berry, J.A., Campbell, P.K., Rascher, U., 2014. Models of fluorescence and photosynthesis for interpreting measurements of solar-induced chlorophyll fluorescence. J. Geophys. Res. Biogeo. 119, 2312–2327.
Van Der Tol, C., Verhoef, W., Timmermans, J., Verhoef, A., Su, Z., 2009. An integrated model of soil-canopy spectral radiances, photosynthesis, fluorescence, temperature and energy balance. Biogeosciences 6, 3109–3129.
Wang, D., Chen, J., Felton, A.J., Xia, L., Zhang, Y., Luo, Y., Cheng, X., Cao, J., 2021. Post-fire co-stimulation of gross primary production and ecosystem respiration in a meadow grassland on the Tibetan Plateau. Agric. For. Meteorol. 303.
Wang, X., Chen, J.M., Ju, W., Zhang, Y., 2022a. Seasonal Variations in Leaf Maximum Photosynthetic Capacity and Its Dependence on Climate Factors Across Global FLUXNET Sites. J. Geophys. Res. Biogeosci. 127, e2021JG006709.
Wang, Y., Kohler, P., Braghiere, R.K., Longo, M., Doughty, R., Bloom, A.A., Frankenberg, C., 2022b. GriddingMachine, a database and software for Earth system modeling at global and regional scales. Sci. Data 9, 258.
Wu, A., Hammer, G.L., Doherty, A., Von Caemmerer, S., Farquhar, G.D., 2019. Quantifying impacts of enhancing photosynthesis on crop yield. Nat. Plants 5, 380–388.
Xie, X., Li, A., Jin, H., Yin, G., Nan, X., 2018. Derivation of temporally continuous leaf maximum carboxylation rate (Vcmax) from the sunlit leaf gross photosynthesis productivity through combining BEPS model with light response curve at tower flux sites. Agric. For. Meteorol. 259, 82–94.
Yang, J., Liu, Z., Yu, Q., Lu, X., 2024. Estimation of global transpiration from remotely sensed solar-induced chlorophyll fluorescence. Remote Sens. Environ. 303, 113998.
Yang, P., Van Der Tol, C., Campbell, P.K.E., Middleton, E.M., 2021. Unraveling the physical and physiological basis for the solar- induced chlorophyll fluorescence and photosynthesis relationship using continuous leaf and canopy measurements of a corn crop. Biogeosciences 18, 441–465.
Yang, X., Tang, J., Mustard, J.F., Lee, J.-E., Rossini, M., Joiner, J., Munger, J.W., Kornfeld, A., Richardson, A.D., 2015. Solar-induced chlorophyll fluorescence that correlates with canopy photosynthesis on diurnal and seasonal scales in a temperate deciduous forest. Geophys. Res. Lett. 42, 2977–2987.
Ye, Z.P., 2010. A review on modeling of responses of photosynthesis to light and CO2. Chin. J. Plant Ecol. 34, 727–740.
Ye, Z.P., Yu, Q., 2007. Comparison of a new model of light response of photosynthesis with traditional models. J.-Shenyang Agric. Univ. 38, 771.
Ye, Z.P., Yu, Q., 2008. Comparison of new and several classical models of photosynthesis in response to irradiance. J. Plant Ecol. 32, 1356–1361.
Yin, X., Struik, P.C., 2009. C3 and C4 photosynthesis models: An overview from the perspective of crop modelling. NJAS Wageningen J. Life Sci. 57, 27–38.
Yu, L., Luo, X., Croft, H., Rogers, C.A., Chen, J.M., 2024. Seasonal variation in the relationship between leaf chlorophyll content and photosynthetic capacity. Plant. Cell. Environ. 47, 3953–3965.
Zheng, T., Chen, J., He, L., Arain, M.A., Thomas, S.C., Murphy, J.G., Geddes, J.A., Black, T.A., 2017. Inverting the maximum carboxylation rate (Vcmax) from the sunlit leaf photosynthesis rate derived from measured light response curves at tower flux sites. Agric. For. Meteorol. 236, 48–66.
Zhu, T.T., Li, J., Liu, Y.Y., Tong, X.J., Yu, Q., 2020. Leaf photosynthetic light response of summer maize: comparison of models and analysis of parameters. Photosynthetica 58, 19–28.